FREIE UNIVERSITÄT BERLIN

MASTER THESIS

Single Shot Broadband Terahertz Detection

Amon Ruge

Primary Supervisor

Prof. Dr. Tobias Kampfrath

Second Assesor

Prof. Dr. Christian Frischkorn

April 3, 2024

Contents

1 Introduction

Terahertz (THz) spectral range covers frequencies from 0.1 to 50 THz [1]. Due to its photon energy, THz radiation is a powerful tool for low-energy excitations. The excitation of spin-waves [2], phonons [3; 4], and ionization of excitons [5] are possible. Additionally, ultrafast spin dynamics can be investigated by the study of THz emission [6].

There are multiple sources to generate THz radiation. Firstly, photoconductive antennas, which are used for linear THz spectroscopy with limited bandwidth <6 THz [7; 8]. Secondly, organic crystals with a bandwidth from 1-10 THz and a major detriment of having gaps in their emission spectrum [9]. Thirdly, the lithium niobate crystal ($LiNbO_3$) with a bandwidth of 0.1-2.5 THz creates high peak amplitudes for non-linear THz spectroscopy [10; 11]. Lastly, the spintronic terahertz emitter covers a range of 0.3-15 THz [12] and was recently improved to match its peak amplitude to the commonly used $LiNbO_3$ [13].

With regards to detection, usually electro-optic sampling (EOS) using a pump-probe scheme is utilized [14]. With this, a multi-shot approach is used by which the timing between the THz pump and probe is modified to measure the temporal change in the refractive index of the material, which is proportional to the THz amplitude [15]. This approach has some disadvantages. The shot-to-shot fluctuations (noise) of the multiple sampling pulses may easily exceed small signal amplitudes. Therefore, a long averaging time is necessary to obtain an acceptable signal-to-noise ratio. The single-shot EOS (SEOS) could overcome these drawbacks because it requires only one probe pulse to measure the time-resolved change in the refractive index of the material over the whole duration of the THz pulse [17].

This work showcases the successful implementation of a single-shot approach for broadband THz detection. The efficacy of this approach was ascertained through a comparison with the established multi-shot EOS (MEOS) methodology. Furthermore, in order to gain deeper insights into the underlying dynamics at play, theoretical modeling of the SEOS technique was also carried

out. Collectively, these investigations provide a comprehensive understanding of the advantages and limitations offered by the SEOS approach in THz detection.

2 Theory

This chapter provides a thorough theoretical framework for understanding the EOS method. Beginning with a detailed illustration of the THz generation process, the chapter proceeds to delve into the derivation of the electric field of the probe pulse. It is followed by an exploration of the phenomenon of spectral chirping, and its attendant effect on the broadening of the probe pulse, clarified via mathematical discourse. Finally, all these preparatory contemplations are leveraged to provide a theoretical model of the measured signal utilizing the SEOS methodology.

2.1 Pump-probe scheme
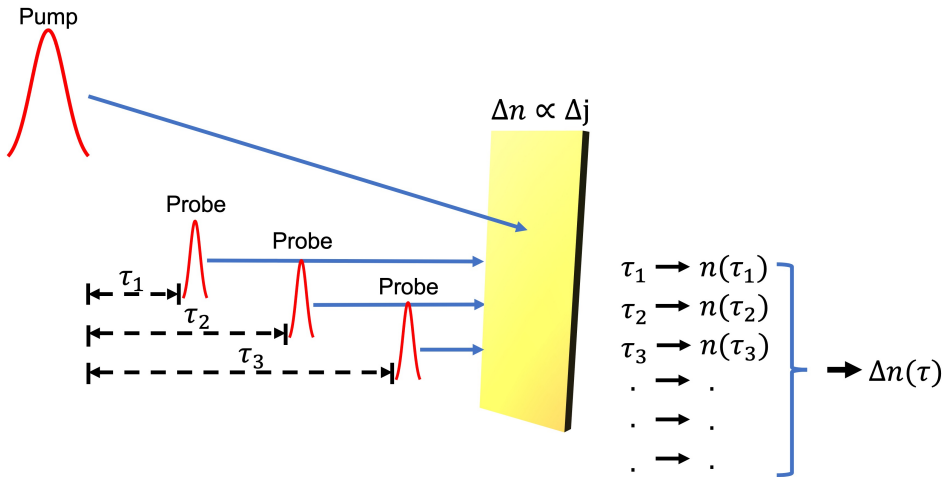
Figure 1 The multi-shot pump-probe can be realized by changing the timing between the pump and probe pulse. By iterating over different delays, the change of an optical constant can be measured over time.

Pump-probe spectroscopy represents a highly versatile and valuable tool for investigating ultrafast dynamics in materials. As its name implies, this technique involves the application of two distinct pulses, a pump pulse, and a probe pulse, which interact with a given sample material. Specifically, the pump pulse serves to initiate a response within the sample, following which the probe pulse can be deployed to monitor the resultant changes induced by the pump (Figure 1). Notably, it is crucial that the probe pulse possesses con-

siderably lower pulse energy than the pump pulse to prevent any inadvertent excitation of dynamics in the sample. In particular, the pump-probe response of the sample is characterized by pump-induced changes Δn in the refractive index n. The change Δn is measured by the probe pulse at a given time difference τ_1 between the pump and probe. By iteration over different time delays τ_1, τ_2, etc., the time evolution of the refractive index $n(\tau)$ can be recorded. To acquire the temporal evolution of dynamics, multiple pump-probe pairs are necessary. Therefore it is a multi-shot approach.
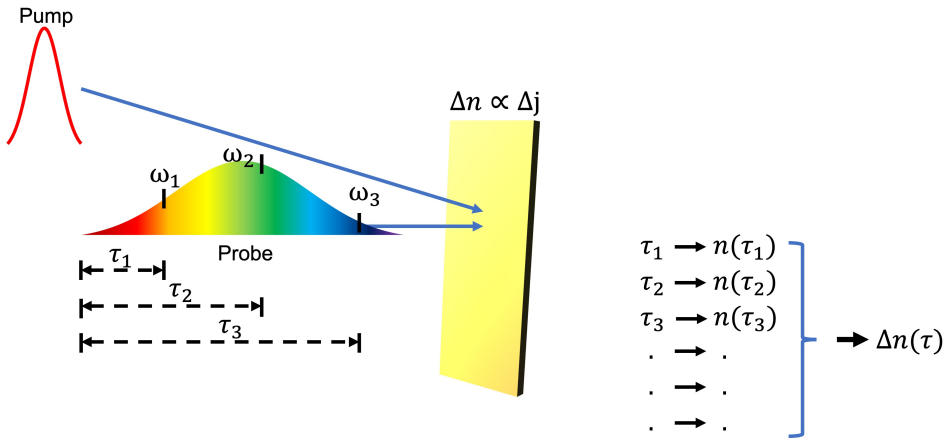

Figure 2 The SSD pump-probe can be realized by chirping the pulse and causing a frequency-dependent phase shift. The chirped pulse interacts with the pulse, causing a change in the probe pulse for different frequencies. Since the frequencies correspond to different timings, the dynamics can be determined with one single shot

A different approach can also be chosen. Instead of measuring the time evolution with multiple shots, one can determine it with one single shot [16]. The fundamental concept underlying the single-shot detection technique is the temporal broadening of the probe pulse, which can be achieved through the phenomenon of dispersion, commonly facilitated by dispersive materials, gratings, or prisms. The dispersion generates a frequency-dependent phase shift, wherein the lower frequency components are situated ahead of the pulse while the higher frequency components are situated at the rear. As a result, every probe frequency component is related to a distinct temporal delay with respect to the pump pulse. Therefore by the spectral encoding of the time, the frequency components can be assigned to time components. This approach has

a significant advantage as the time information of a pulse can be determined by acquiring the temporal information in one shot. In comparison to previous methods, the timing difference is now imprinted in the frequency domain, where a temporal difference τ_1 corresponds to a frequency ω_1, τ_2 to ω_2, and so on, of the probe pulse. Therefore, with one interaction between the pump and probe pulse, each frequency component of the probe undergoes a unique pump-induced current variation in the material.

2.2   Electro-Optic Sampling

In our electro-optic sampling setup, the sample used is a crystal with broken-inversion symmetry. A distinct feature of this symmetry property is that the change in birefringence Δn is directly proportional to the magnitude of the incoming THz electric field E_{THz} due to the Pockels effect. This change can be quantified through second-order polarization, which depends on the susceptibility tensor $\chi^{(2)}$ of the material:

$$\Delta n(t) \propto \chi^{(2)} E_{\text{THz}}(t) \tag{1}$$

In materials that possess broken-inversion symmetry, the susceptibility tensor $\chi^{(2)}$ vanishes, thereby eliminating the other order contributions and leaving only the sum-frequency generation (SFG) and difference-frequency generation (DFG) terms. These second-order terms induce a change in the refractive index through the THz field, which is referred to as the electro-optic or Pockels effect. Thus, the change in susceptibility results in temporary birefringence of the crystal. Consequently, when the probe pulse and the THz field propagate collinearly through the crystal, the probe pulse undergoes a change in its polarization, transforming it from linear polarization to elliptical polarization. The degree of ellipticity is also proportional to the THz field, and therefore the magnitude of the THz field can be determined by measuring the degree of ellipticity.
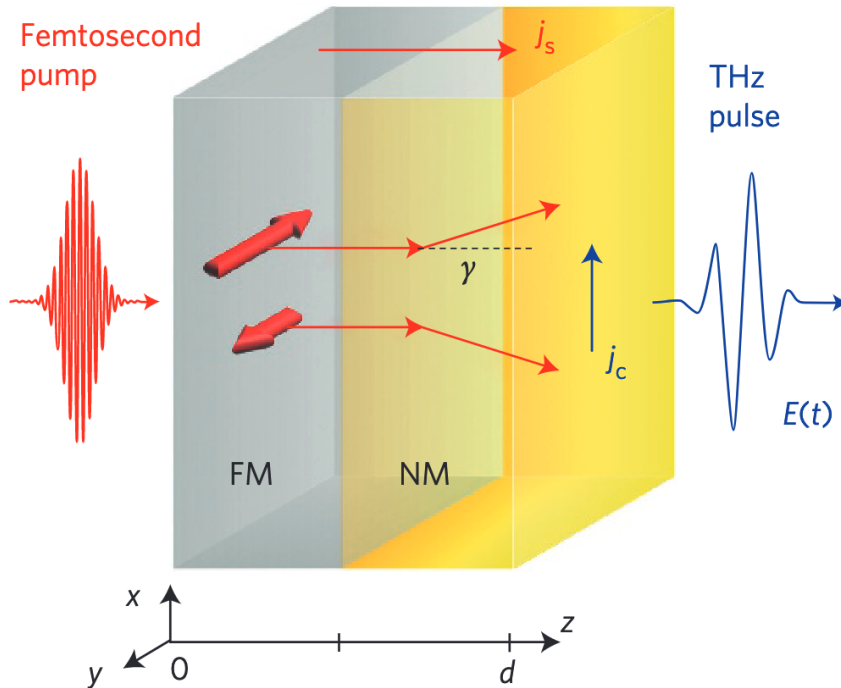
2.3 Spintronic Terahertz Emitter

Figure 3 A femtosecond pulse induces heating in the FM layer, which leads to an ultrafast electron temperature. This excess heat leads to the quenching of magnetization and launches a net spin current in the z-direction to the interface between FM and NM layers. In the NM layer spin-to-charge conversion occurs, which leads to an electric dipole, that emits THz radiation [19].

The generation of the broadband THz pulse from 0.3 up to 30 THz is realized by the spintronic THz emitter (STE) [19]. It consists of two parts, a ferromagnetic (FM) layer, and a nonmagnetic (NM) layer. The FM layer is irradiated with an optical femtosecond laser, which initiates a sequence of events, beginning with the heating of the electrons in the layer. As the magnetization in a ferromagnet is temperature-dependent and follows the Bloch-law [18], the temperature change in the layer causes a change in magnetization. Consequently, this results in a generalized spin voltage $\Delta\mu_s$, a difference between generalized chemical potentials of spin-up and spin-down electrons [20]. The system seeks to dissipate the excess magnetization, leading to two main mechanisms: an ultrafast demagnetization by spin flips, $\dot{M}$, and a net spin current, j_s, in the z-direction towards the interface between the two layers. The NM layer is made of material with strong spin-orbit coupling, which is responsible for

8

the inverse spin-Hall effect (ISHE) resulting in the deflection of spin-up and spin-down electrons. Since the current is spin-polarized, the ISHE leads to an imbalance in the proportion of majority and minority spins at the interface, leading to an imbalance in the proportion of electrons deflected in the positive and negative x-directions. Resulting in-plane charge current in the x-direction j_c which can be described as $j_c = \gamma j_s$ with γ being the spin-Hall angle [21]. Finally, the charge current j_c serves as a source of the THz radiation [19].

$$E(t) \propto j_c(t) \tag{2}$$

2.4 Spectral chirping

As is customary in optics, we will commence our analysis by considering Maxwell's equations to gain insight into the nature of our probe pulse. The first two Maxwell equations are the divergence of the E and B-field while the latter two describe the curl of the electric and magnetic fields, namely Faraday's law and Ampere's law, respectively. Since both laws have a B-field contribution we apply a time derivative $\partial/\partial t$ to Ampere's law and the curl of Faraday's law to eliminate this magnetic field contribution. In consequence, we arrive at the Helmholtz equation [23].

$$\boldsymbol{\nabla} \times \boldsymbol{\nabla} \times \boldsymbol{E} + \frac{1}{c^2} \frac{\partial^2}{\partial t^2} \boldsymbol{E} = -\frac{4\pi}{c^2} \frac{\partial}{\partial t} \boldsymbol{j} \tag{3}$$

The current is the time derivative of the polarizability $\boldsymbol{P}$. It is a functional that depends on the electric field. The electric fields inside the atoms of solid materials are of the order of $10^9 \, \frac{\text{V}}{\text{cm}}$ [24]. In contrast, the electric fields used in this work are at least three magnitudes smaller around $1 \frac{\text{MV}}{\text{cm}}$. On this basis, the assumption can be made that the electric fields are only a small perturbation compared to the electric fields inside the atoms. Therefore, we can Taylor expand the polarizability around $\boldsymbol{E}$.

$$\boldsymbol{P}[\boldsymbol{E}] = \chi^{(1)}\boldsymbol{E}^{(1)} + \chi^{(2)}\boldsymbol{E}^{(2)} + \cdots \tag{4}$$

If we assume a linear response, where the electric field $\boldsymbol{E}$ is the perturbation, the susceptibility χ the response, and the polarizability $\boldsymbol{P}$ is the reaction, we can write the polarizability as a convolution between the susceptibility and the electric field. This can be more easily evaluated in the frequency domain by Fourier transformation since it simplifies to a multiplication:

$$\tilde{\boldsymbol{P}}(\omega) = \tilde{\chi}(\omega)\widetilde{\boldsymbol{E}}(\omega) \tag{5}$$

Additionally, we define three quantities:

$$k(\boldsymbol{x}, \omega) = \frac{n(\boldsymbol{x}, \omega)\omega}{c} \tag{6}$$

$$n = \sqrt{\epsilon} \tag{7}$$

$$\epsilon = 1 + 4\pi\chi \tag{8}$$

where k is the wavenumber, the n refractive index, and ϵ the dielectric functions. Additionally, we assume that n is constant and consequently homogenous:

$$\left(\boldsymbol{\nabla} \times \boldsymbol{\nabla} \times \cdot + k^2\right)\boldsymbol{E} = \frac{4\pi\omega^2}{c^2}\boldsymbol{P} \tag{9}$$

On the left next to the electric field $\boldsymbol{E}$ is a linear operator that describes the evolution $\boldsymbol{E}$. If we take nonlinear effects into account, we have a non-vanishing polarizability $\boldsymbol{P}$ and can describe effects like sum- and difference-frequency generation. These effects are essential for the pump-probe experiment. But for the description of the chirping, we only regard the linear part. On this basis, we can simplify the Helmholtz equation for isotropic media as follows:

$$\left[\nabla^2 + k^2(\boldsymbol{x},\omega)\right]\boldsymbol{E}(\boldsymbol{x},\omega) = 0 \tag{10}$$

Now we can write the electric field as a superposition of plane waves, which are solutions of the above Helmholtz equation. From that, the angular spectrum representation or plane wave expansion can be used to describe the electric field [23].

$$\mathbf{E}(x,y,z) = \frac{1}{2\pi}\int_{-\infty}^{\infty}\int_{-\infty}^{\infty}\mathbf{E}\left(k_x,k_y;z=0\right)e^{i[k_x x+k_y y]}e^{i[\pm k_z z]}\mathrm{d}k_x\mathrm{d}k_y \tag{11}$$

This system connects $\mathbf{E}(x,y,z=0)$ to $\mathbf{E}(x,y,z)$ by a convolution because it exhibits translational invariance along the x- and y-directions. In Fourier space (k_x,k_y) if the electric field is known at a given position $\mathbf{E}(k_x,k_y,z)$, the field at a later position $\mathbf{E}(k_x,k_y,z+L)$ can be determined by multiplying with a transfer function called the propagator $e^{i[\pm k_z z]}$. The $\pm$ sign describes the propagation in the $z>0$ direction and in the $z<0$ direction. In this context, we are only interested in the fields behind the source, so we only consider the positive sign. For simplification, we assume $k_x = k_y = 0$, i.e. the wave propagates along the z direction. In addition, the phase ϕ can be introduced and be described as a multiplication between the wavevector k and the spatial coordinate z as $\phi = kz$. In the time domain, we thus have

$$\mathrm{E}(z,t) = \frac{1}{2\pi}\int\tilde{E}(z=0,\omega)e^{i\omega t}e^{i\phi}d\omega \tag{12}$$

It describes the initial electric field at a position $z=0$ in the frequency domain, which gets multiplied by the propagator $e^{i\phi}$. Here, the propagator describes the evolution of the electric field in the frequency domain during its propagation. This can then be Fourier transformed to obtain the electric field in the time domain. If there is no attenuation, kz and ϕ are real-valued, and the propagator is just a phase factor. The phase can be Taylor expanded for small

frequencies around its center frequency ω_0

$$\phi(\omega) = \phi_0 + (\omega - \omega_0)\left(\frac{d\phi(\omega)}{d\omega}\right)_{\omega_0} + \frac{1}{2!}(\omega - \omega_0)^2\left(\frac{d^2\phi(\omega)}{d\omega^2}\right)_{\omega_0} + O\left(\omega^3\right) \quad (13)$$

The phase consists of three terms. The first part is the absolute phase ϕ_0, which is the phase accumulated around the center frequency ω_0. The second part is the first derivative $\phi_0' = (\frac{d\phi}{d\omega})_{\omega_0}$, which is the group delay. This causes a shift in time and can be intuitively understood by inserting $\phi = kz$. Then it describes the inverse of the group velocity $(\frac{d\omega}{dk})^{-1}$ multiplied by a distance z. The last part of the Taylor expansion is the second derivative $\phi_0'' = (\frac{d^2\phi}{d\omega^2})_{\omega_0}$, the group delay dispersion (GDD), and induces the temporal broadening of the pulse. The GDD is highly important for our purposes, as we intend to chirp the pulse. This can be achieved using a dispersive medium, a pair of gratings, or prisms. For a better understanding of the pulse change by introducing a dispersion, we assume that the initial pulse is a Fourier-limited Gaussian [25].

$$\tilde{E}(0, \omega) \propto \exp\left(-\frac{(\omega - \omega_0)^2}{\Delta\omega^2}\right) \quad (14)$$

With $\Delta\omega$ describing the width of the Gaussian pulse. This assumption can be inserted into the equation of the electric field.

$$E(z, t) \propto \int d\omega \exp\left(-\frac{(\omega - \omega_0)^2}{\Delta\omega^2}\right)\exp(i\phi - i\omega t) \quad (15)$$

By inserting the expression of the Taylor expansion of the phase, the electric field can be described differently.

$$E(z, t) \propto \int d\omega \exp\left(-\frac{(\omega - \omega_0)^2}{\Delta\omega^2} - (i\omega t - i\omega_0 t) - i\omega_0 t + i\phi_0\right.$$
$$\left. + i\phi_0'(\omega - \omega_0) + \frac{1}{2}\phi_0''(\omega - \omega_0)^2\right) \quad (16)$$

In order to solve the integral more easily, the integration variable can be

changed to $u = \omega - \omega_0$ With this preparatory work, the following relationship can be used in order to solve the integral [23]:

$$\int_{-\infty}^{\infty} \mathrm{d}x \exp\left(-ax^2 + bx + c\right) = \sqrt{\frac{\pi}{a}} \exp\left(\frac{b^2}{4a} + c\right) \tag{17}$$

From that, we finally can find an expression of the electric field in the time domain:

$$E(z,t) \propto \sqrt{\frac{\pi}{\Delta\omega^{-2} - \frac{1}{2}\phi''}} \exp\left(\frac{-(\phi_0' - t)^2}{4\left(\Delta\omega^{-2} - \frac{1}{2}\mathrm{i}\phi''\right)}\right) \exp\left(-\mathrm{i}\omega_0 t + \mathrm{i}\phi_0\right) \tag{18}$$

This equation has three factors. The first term, which results in a decrease in the amplitude of the pulse, is attributed to the principle of conservation of energy. As the pulse broadens, to maintain constant energy, the amplitude has to decrease. The second term corresponds to the Gaussian envelope of the beam, which determines the shape and broadness of the pulse. Finally, the carrier wave describes the temporal and spatial modulation of the wave. The equation (18) can be rewritten as

$$E(z,t) \propto \sqrt{\frac{\pi}{\Delta\omega^{-2} - \frac{1}{2}\phi''}} \exp\left(\frac{-(\phi_0' - t)^2}{(4\Delta\omega^{-2} - \Delta\omega^2\phi''^2)}\right)$$
$$\exp\left(\mathrm{i}(\phi_0 - \omega_0 t) + \mathrm{i}\alpha\left(\phi_0' - t\right)^2\right) \tag{19}$$

Here the α is defined as the laser chirp rate [22]

$$\alpha = \frac{\phi''}{8\Delta\omega^4 + 2\phi''^2} \tag{20}$$

The chirp rate describes the rate at which the frequency of a signal changes over time and is the time derivate of the instantaneous frequency ω_{inc}.

$$\alpha = \frac{\partial\omega_{\mathrm{inc}}}{\partial t} \tag{21}$$

The instantaneous frequency refers to the frequency of a signal at any given

point in time, which varies if dispersion is present. The result of equation (19) shows that in the time domain, the chirp pulse has a slowly varying envelope and fast oscillating phase $e^{i\alpha t^2}$ for a sufficiently large α.

2.5   Pulse length

Of all the aspects of the Taylor expansion, the frequency chirping and the alteration of pulse length through the GDD stand out as the most captivating for our purposes. The Gaussian assumption in frequency is introduced in the equation (14). By carrying out a Fourier transform from the frequency domain to the time domain, the Gaussian pulse in time is determined.

$$E(z,t) \propto \exp\left(\frac{-t^2}{4\Delta\omega^{-2}}\right) \tag{22}$$

Additionally, the pulse length τ_0 of a Gaussian electric field is commonly defined as the full with at half maximum (FWHM) of the intensity in the time domain.

$$I(z,t) \propto |E(t)|^2 = \exp\left[-4\ln 2\left(\frac{t}{\tau_0}\right)^2\right] \tag{23}$$

Using equation (23), the pulse duration can be computed by ascertaining the width of the Gaussian pulse in the frequency domain. It should be noted that the Fourier limited pulse width represents the minimum possible pulse duration for a given spectral bandwidth.

$$\tau_0 = \sqrt{\frac{8\ln 2}{\Delta\omega^2}} \tag{24}$$

An analogous procedure can be applied to the analysis of chirped pulses by adjusting the pulse duration to τ_c and utilizing equation (18). This approach leads to a correlation between the coefficients, which can be determined

through a comparison process, assuming that the group delay is negligible.

$$\tau_c = \tau_0 \sqrt{1 + \left(\frac{4\ln 2\phi''}{\tau_0^2}\right)^2} \tag{25}$$

The equation presented above demonstrates that a pulse undergoes greater proportional stretching as its duration decreases. Moreover, if it is desirable to stretch a pulse using a material, a strongly dispersive medium with a substantial thickness is required. The GDD for dispersive materials can be easily determined using the phase relationship $\phi = kz = kL$, where L denotes the thickness of the material and can be used as a substitute for the distance z, which is the distance over which the light beam experiences the change in phase. The second derivative of this relationship over the frequency ω yields the following expression.

$$\frac{d^2\phi}{d\omega^2} = \frac{\lambda^3 L}{2\pi c^2} \frac{\partial^2 n}{\partial \lambda^2} \tag{26}$$

For example, an SF10 glass has the following value for the second derivative of the refractive index with respect to the wavelength of [26]

$$\left.\frac{\partial^2 n}{\partial \lambda^2}\right|_{800 \text{ nm}} = 0.176 \frac{1}{\mu\text{m}^2} \tag{27}$$

Consequently, in order to generate a 2 ps pulse starting from an initial 40 fs pulse, SF10 glass with a thickness of 19 cm would be required. However, this approach is both impractical and inconvenient to implement in an experimental setup, and controlling the thickness of the material to regulate the GDD presents a significant challenge. Therefore, an alternative approach must be pursued to achieve the desired results.

2.6 Grating principle

By the usage of a pair of grating, an angular dispersion and, thus, frequency dispersion can be achieved as visible in Figure 4 (a). This can be realized

through a simple configuration of two opposing gratings, where the longer wavelength components of the light travel a farther distance than the shorter wavelength components. Therefore, a pair of gratings induce a negative dispersion or negative GDD. In contrast, the utilization of a dispersive medium leads to a positive dispersion. There the short wavelength components are in front of their longer counterparts. This can also be accomplished by the insertion of a lens between two gratings [28]. Based on the shape of the lens in use, the shape of the beam can be manipulated, and the type of dispersion. In our work, we focused on the simple and classical setup with two gratings, introduced by Treacy [27] The phenomenon and the resulting equation of the grating can be simply described by Huygens's principle. Assuming a monochromatic plane wave encountering the grating at normal incidence. Each slit of the grating acts like a point-like source, propagating in all directions. The resulting spherical waves from each slit interfere constructively or destructively. The intensity maxima occur if the following relationship is fulfilled [26].

$$d \sin \theta_m = m\lambda \tag{28}$$

Whereby d is the distance between two adjacent slits, θ_m the diffraction angle, m is the order and lastly, there is the wavelength λ. The order m can only adopt integer values. In our case, the incident light is not normal to the grating surface, hence we must incorporate an incident angle θ_i of the incoming light.

$$\sin \theta_m = m\frac{\lambda}{d} + \sin \theta_i \tag{29}$$

The gratings are used in the Littrow configuration, which means that the diffracted beam goes back to where the incoming beam came from. This allows for higher efficiency of the gratings since generally blazed gratings are optimized for it. In addition, we also utilized transmission gratings, where we

have a slightly changed geometry.

$$\sin \theta_m = m\frac{\lambda}{d} - \sin \theta_i \tag{30}$$

Overall, the phase shift originating from the gratings can be separated into two contributions. The first is determined by the path P the light travels through the gratings, which is illustrated by Figure 4
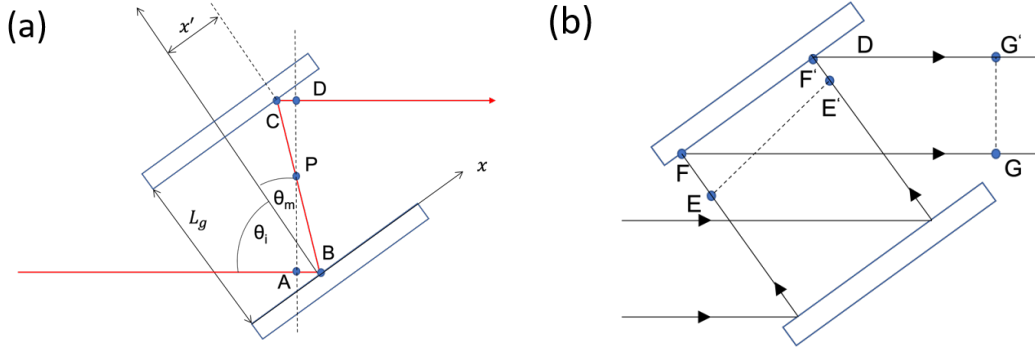

Figure 4 (a) The light path in the two gratings can be described by $ABCD$. (b) After the two gratings, a phase matching must occur so that the wavefront has the same phase.

The path of light through the grating pair can be divided into three different segments.

$$\overline{ABCD} = \overline{AB} + \overline{BC} + \overline{CD} \tag{31}$$

Whereby the path $\overline{AB}$ and $\overline{BC}$ can be expressed with the diffraction angle θ_i and θ_m

$$\overline{AB} = \overline{BP}\cos\left(\theta_i + \theta_m\right) \tag{32}$$

$$\overline{CD} = \overline{CP}\cos\left(\theta_i + \theta_m\right) \tag{33}$$

Figure 4 (a) exemplifies that $\overline{BP} + \overline{CP} = \overline{BC}$ and with that, a condensed expression can be found.

$$\overline{ABCD} = \overline{BC}\left(1 + \cos\left(\theta_i + \theta_m\right)\right) \tag{34}$$

17

The distance between points B and C can be expressed through the distance L_g between the two gratings and a final expression for the path length can be found.

$$P = \frac{L_g}{\cos\theta_m} \left[1 + \cos\left(\theta_m + \theta_i\right)\right] \tag{35}$$

However, it is important to consider another contributing factor - the grating phase shift, which can be interpreted as a phase correction arising from the characteristics of the grating. As depicted in Figure 4 (b), a wavefront EE' with a constant phase encounters the second grating. The wavefront preserves its properties following its passage through the grating, as illustrated by its evolution GG', where the tilted wavefront is planar again after passing the second grating. Notably, a significant discrepancy can be observed when comparing the paths $\overline{EFG}$ and $\overline{E'F'G'}$, which must be compensated for at the grating surface FF'. To achieve this, a phase matching process is necessary, which can be expressed as a correction of 2π multiplied by the number of rulings in x'[27].

$$\phi_g\left(x'\right) = m\frac{2\pi}{d}x' \tag{36}$$

The total wave-dependent can then be described by the addition of the grating phase matching ϕ_g and the phase caused by the traveling distance.

$$\phi = \frac{\omega}{c}n_{\text{Air}}P + \phi_g\left(x'\right) \tag{37}$$

In the first addend, we insert for the traveling distance the path of light P. Additionally, we assume that the refractive index of air is $n_{\text{Air}} \approx 1$ [29]. By taking the second derivative of the wave-dependent phase shift, the GDD can be determined.

$$\frac{d^2\phi}{d\omega^2} = -\frac{\lambda^3 L_g}{\pi c^2 \Lambda^2}\left[1 - \left(\frac{\lambda}{d} - \sin\theta_i\right)^2\right]^{-3/2} \tag{38}$$

18

The analysis of the GDD reveals that the grating configuration always introduces a negative chirp. The reason behind it is due to two factors. Firstly, all variables in the equation are positive except for the angle θ_i, resulting in the left part of the multiplicand being always positive. Secondly, the expression in the brackets can be reformulated using the relationship between the incoming light angle θ_i and the outgoing angle θ_m in equation (29), along with the fact that $\sin^2 \theta_i + \cos^2 \theta_i = 1$. We obtain

$$\left[1 - \left(\frac{\lambda}{d} - \sin \theta_i \right)^2 \right]^{\frac{1}{2}} = \cos \theta_m \tag{39}$$

Since the reflected beam has to lie in the incident half space of the grating, the possible values for the angles are $\theta_m \in \left[-\frac{\pi}{2}, \frac{\pi}{2} \right]$. This leads to the fact, that the cosine is always positive and therefore to the conclusion that the term in the brackets in the equation (38) is also positive. As a result, the GDD is always negative for the pair of gratings. This is the reason, why they are called compressor because it counteracts the positive dispersion caused by dispersive media.

All in all, the GDD can be varied by keeping all the variables constant, i.e. using the same pair of grating and angle of incidence, except the distance L_g between the gratings which we can change.

If the grating introduces higher-order dispersion, the chirp can not be regarded as linear anymore. Therefore, it is useful to investigate these terms. The third-order dispersion term is expected to exhibit the most significant impact. The calculation of this term requires differentiation of the GDD equation in (38) with respect to the frequency variable ω, yielding

$$\frac{d^3\phi}{d\omega^3} = -\frac{d^2\phi}{d\omega^2} \frac{3\lambda}{\pi c} \frac{1 + \frac{\lambda}{d} \sin \theta_i - \sin^2 \theta_i}{1 - \left(\frac{\lambda}{d} - \sin \theta_i \right)^2} \tag{40}$$

This shows, that the third-order term increases if the second-order, the GDD, also increases. To put it in another way, the GDD is proportional to the

grating distance L_g and therefore the third-order term would also increase proportionally to it as well.

2.7 Single-shot response

In this chapter, we want to describe the response of our system to an incoming THz field to understand the underlying dynamics. The signal on the spectrometer depends on the contribution of the ΔE_{probe} and the E_{probe}. ΔE_{probe} describes the pump-induced change due to the interaction between the THz field and the probe field. E_{probe} is the electric field of the unperturbed part of the probe and has a much higher amplitude than ΔE_{probe}. Therefore it is regulated by an analyzer, which is accounted for by a factor C. It has its maximum at one when the transmission axis is parallel to the E_{probe} and its minimum at zero when parallel to the extinction axis of the polarizer. In the experiment, the extinction axis of the polarizer deviates slightly from the probe polarization direction, by a few degrees, and factor C has a magnitude of a few percent. The signal measured on the spectrometer can be then described in the following way:

$$\Delta S(\omega) \propto \left| \mathcal{F} \left(\Delta E_{\text{probe}} \left(t \right) + C E_{\text{probe}} \left(t \right) \right) \right|^2 \tag{41}$$

The spectrometer performs a Fourier transformation of the time-dependent pump-induced and probe electric field and measures the intensity. This signal can be then reshaped to

$$\Delta S(\omega) \propto 2 \operatorname{Re} \left(\Delta \tilde{E}_{\text{probe}} \, C^* \tilde{E}^*_{\text{probe}} \right) + \left| \Delta \tilde{E}_{\text{probe}} \right|^2 + C^2 \left| \tilde{E}_{\text{probe}} \right|^2 \tag{42}$$

This result indicates a pronounced dependence of the measured signal on the electric field of the probe since it has a quadratic contribution in addition to the linear one. To mitigate the effect of the quadratic E_{probe} component, signals obtained with opposing E_{THz} polarization can be subtracted. The reversal in THz polarization can be achieved by switching the direction of the external

20

magnets located adjacent to the STE. The subtraction results in:

$$S_{\text{SEOS}} \propto \Delta S\left(E_{\text{THz}}\right) - \Delta S\left(-E_{\text{THz}}\right) \propto 4\,\text{Re}\left(\Delta \tilde{E}_{\text{probe}}\, C^* \tilde{E}_{\text{probe}}^*\right) \qquad (43)$$

In the end, only the linear terms remain and therefore the pump-induced change can be directly measured by the spectrometer. In addition, the SEOS signal S_{SEOS} also depends on the probe's electric field. Therefore, the measured signal always contains the chirp information. The E_{probe} component can be computed by using the derivations used above knowing the GDD.

2.8 The simple model of EOS

The pump-induced change, when the THz and the probe beam propagate collinearly through the crystal, can be described in a simple model in the time domain by the following multiplication:

$$\Delta E_{\text{probe}}(t) = E_{\text{THz}}(t + \tau)E_{\text{probe}}(t) \qquad (44)$$

The timing between the THz pulse and the probe pulse is varied through a delay τ. When Fourier transforming, it results in

$$\Delta E_{\text{probe}}(\omega) = \int_{-\infty}^{\infty} d\Omega\, E_{\text{THz}}(\Omega)E_{\text{probe}}(\omega - \Omega)e^{i\Omega\tau} \qquad (45)$$

with ω and Ω describing the optical and THz frequencies, respectively. The probe pulse contains the phase factor $e^{i\phi}$ in which the dispersion is encoded. The change in timing between the probe and THz field through the delay τ is described in the frequency domain by the $e^{i\Omega\tau}$ term. Assuming the probe pulse to be a δ-like peak, the equation (45) would shift the THz electric field from the THz frequencies Ω to the optical frequencies ω. However, in practical scenarios, the probe electric field is not a δ-like peak and has a Gaussian-like shape, which leads to a frequency-domain windowing of the THz electric field depending on the width of the Gaussian. Moreover, the probe has an additional chirp in our SEOS methodology. The presence of a chirp in the probe electric
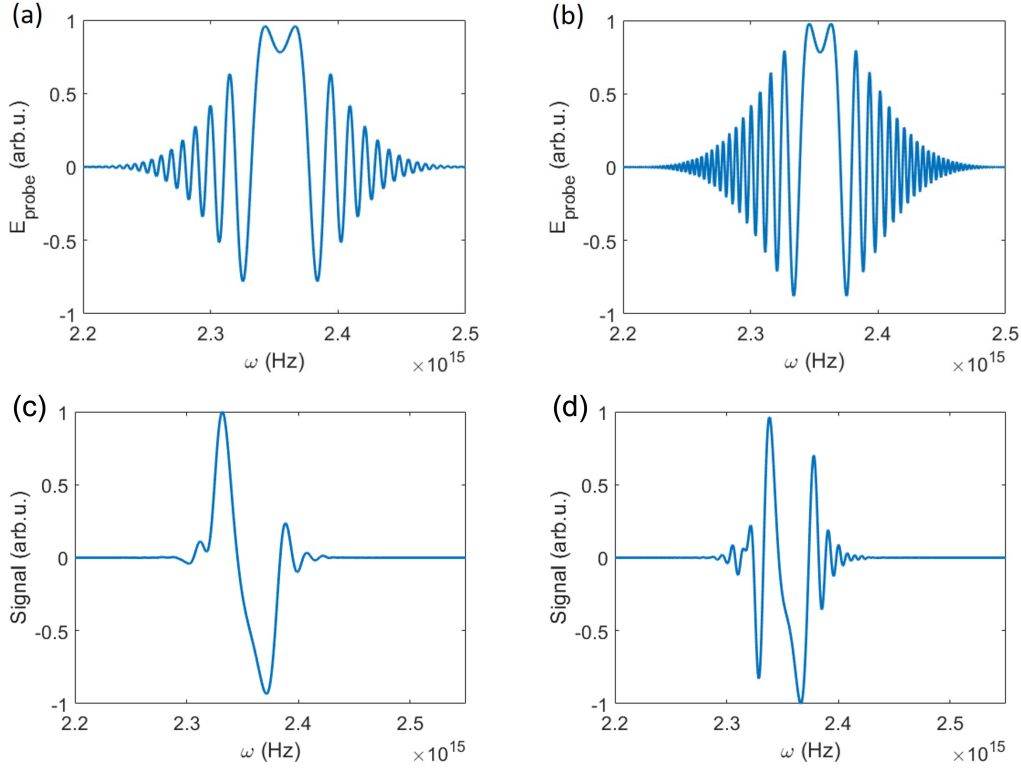
Figure 5 (a) Modeled chirped probe pulse for an initial Gaussian-shaped pulse (a) and with increased GDD by a factor of 2 (b). Modeled signals based on the convolution assumption for ΔE_{probe} (c) and with increased GDD by a factor of 2 (d).

field gives rise to oscillations in the electric field, which become more prominent with increasing GDD values due to its dependence on $\phi_0''(\omega - \omega_0)^2$, as discussed in section (2.4). Specifically, as the GDD increases with the squared frequency, the phase oscillations become stronger further away from the center frequency ω_0. This phenomenon is illustrated in figures 5(a) and 5 (b), where the GDD is increased by a factor of 2, resulting in stronger oscillations in the real part of the electric field. As a result, the frequency-dependent phase shift is larger, causing a greater time difference between the individual frequencies. Upon evaluation of the signal for two different values of GDD, as shown in Figure 5 (c) and (d), two distinct results are observed. These differences are commonly attributed to distortions of the single-shot technique, which are characterized by a longer single cycle and additional oscillations with higher amplitude and imply that the simple mapping of the instantaneous frequencies to time $\omega_{\text{inc}} \leftrightarrow t$ does not work. Here, we retrieved the THz spectrum from the MEOS measurements,

the details will be discussed in a later section. The reasoning behind the longer single cycle can be explained by the fact that in the frequency domain, different GDD values only slightly affect the convolution between the THz field and the probe, as the envelope of the probe pulse remains the same. However, the frequency-dependent phase shift leads to a longer signal in the time domain, thus a different translation of the signal from the frequency to the time domain. The stronger oscillation amplitudes are a result of the convolution with a stronger oscillating probe pulse and increasing amplitude towards the center frequency. This highlights the importance of the choice of probe pulse length, as it can lead to signal distortion.

Later in the experimental results, the effect of distortion caused by a longer probe pulse is showcased. These distortions are not caused by the detection of the crystal, since the non-linear effects of the crystal are omitted in equation (45). They originated simply from the technique of encoding a THz pulse on a broad probe pulse.

Using this simple model, we can determine the theoretical conversion from frequency to time. Starting from equation (44) , we can write

$$\Delta E_{\mathrm{probe}} = \int_{-\infty}^{\infty} \mathrm{d}t E_{\mathrm{THz}}(t - \tau) A_{\mathrm{probe}}(t) e^{i\phi(t)} e^{i\omega t} \tag{46}$$

where A_{probe} is the envelope of the probe pulse. We can utilize the method of stationary phase since the term $e^{i(\phi(t)+\omega t)}$ oscillates much more strongly than the THz pulse and the envelope of the probe pulse [25]. The phase factor gives a self-canceling oscillation, except where the time derivative of the exponent is zero. Using the derivation from equation (18), we can write the following expression for the conversion from to time as

$$t = \frac{\omega_{\mathrm{inc}} - \omega_0}{2\alpha} \tag{47}$$

with ω_0 as the center frequency and α as the laser chirp rate. This enables us to determine theoretically, the time information from the SEOS signal on the spectrometer. For that, it requires the determination of the GDD and the

initial pulse width before chirping.

2.9 Detailed modeling of EOS

In reality, the pump-induced change depends on various factors inside the detection crystal, when the THz pulse and the probe beam propagate collinearly through it. The pump-induced change can be described by the following equation [30]

$$\Delta E_{\text{probe}}(\omega) = 4\pi i \frac{\omega^2 t_{23}(\omega)}{c^2 k(\omega)} \int_{-\infty}^{\infty} \mathrm{d}\Omega \, E_{\text{inc}}^{\text{THz}}(\Omega) E_{\text{probe}}(\omega - \Omega) e^{i\Omega\tau}$$
$$\cdot \chi^{(2)}(\omega - \Omega, \Omega) t_{12}(\omega - \Omega) t_{12}(\Omega) \frac{\exp(\mathrm{i}\Delta k d) - 1}{\Delta k} \quad (48)$$

The $\chi^{(2)}$ susceptibility tensor has non-zero elements in crystals with broken inversion symmetry. The symmetry of the $\chi^{(2)}$ tensor sets the THz and probe polarizations required to observe the linear electro-optic effect [31]. The difference frequency generation (DFG) of the second-order polarization [32] is expressed by the difference between the optical ω and THz frequencies Ω. However, the DFG process is restricted by the 'phase matching' condition [33], expressed by the last term in equation (48). It arises from the summation of the spatially expanding spherical waves and maximizes if the product between spatial frequency mismatch Δk and the thickness d is small [34].

$$|\Delta k d| \ll 1 \text{ with } \Delta k = k(\Omega) + k(\omega - \Omega) - k(\omega) \quad (49)$$

If the traveling distance in crystal pulses is short, phase matching should not have a strong influence. The Fresnel transmission coefficients are defined as

$$t_{23}(\omega) = \frac{2n_2(\omega)}{n_2(\omega) + n_3(\omega)} \quad (50)$$

Where n_j is the refractive index of medium 1 (medium of incidence), 2 (electro-optic material), and 3 (substrate). By identifying all these terms of the detection crystal, the pump-induced change and therefore the signal measured with

SEOS can be computed.

2.10 The response function of the system

Our SEOS can be seen as a linear system in which the input power is suffi-
ciently low and acts as a small perturbation, therefore the relationship between
the input and output power can be described as linear. This allows for its char-
acterization by the generalized convolution [35].

$$E_{\text{out}}(t) = \int \mathrm{d}t' H(t, t') E_{\text{in}}(t') \tag{51}$$

It demonstrates that the output functional depends on the time t' and simul-
taneously the input $E_{\text{in}}(t')$. The impulse response function $H(t, t')$ can be
described as a response to a δ-like kick and depends on the time of output t
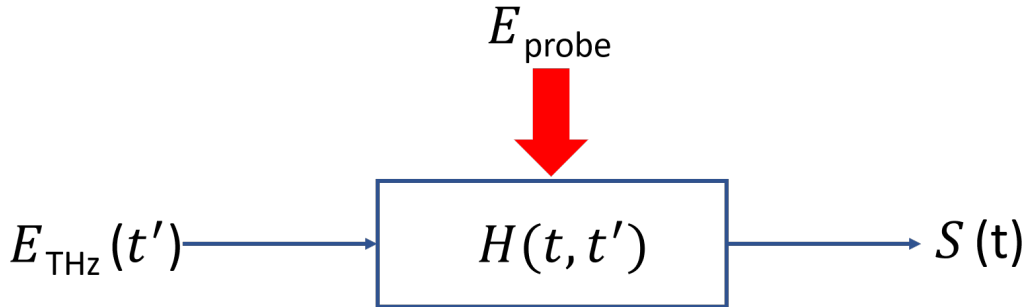and also on the time of input t'.

Figure 6 Schematic picture of an abstract black-box system describes the measured
signal $S(t)$ as a reaction of the incoming THz electric field $E_{\text{THz}}(t')$. The response
function $H(t, t')$ characterizes this linear system which includes the E_{probe}.

Identifying the response function is highly desirable since it contains all
the relevant system information. If the system is in addition time-invariant,
it can be described as a simple convolution [36]. This is the case for the
MEOS methodology, but not for the SEOS. The experimental results will
show, that if the timing between the incoming THz E_{THz} and the probe field
E_{probe} is changed, the waveforms also change and therefore the time invariance
is invalid. Figure (6) depicts the situation for the SEOS. In our case, the
incoming electric field is E_{THz} and the outgoing field is the measured SEOS

signal $S(t)$. By changing the timing τ of THz electric field, the convolution can be written in the following way:

$$S(t, \tau) = \int dt' H(t, t') E_{\text{THz}}(t' + \tau) \tag{52}$$

The observed signal depends on the delay of the THz electric field, as indicated by its dependence on the variable τ. To obtain the desired frequency representation, a two-step Fourier transformation process is employed. Firstly, we Fourier transform with respect to the first variable t, denoted by $\mathcal{F}_1$,

$$\mathcal{F}_1 S(\omega, \tau) = \int dt' \mathcal{F}_1 H(\omega, t') E_{\text{THz}}(t' + \tau) \tag{53}$$

Secondly, we perform another Fourier transformation with respect to the delay τ, denoted by $\mathcal{F}_{12} = \mathcal{F}_1 \mathcal{F}_2$.

$$\mathcal{F}_{12} S(\omega, \Omega) = \int dt' \mathcal{F}_1 H(\omega, t') \mathcal{F}_2 E_{\text{THz}}(\Omega) e^{i\Omega t'} \tag{54}$$

where the integral is just a Fourier transformation with respect to t'. We can rewrite the result as

$$\mathcal{F}_{12} H(\omega, \Omega) = \frac{\mathcal{F}_{12} E_{\text{out}}(\omega, \Omega)}{\mathcal{F}_2 E_{\text{in}}(\Omega)} \tag{55}$$

In essence, the SEOS technique enables the determination of the response function of a system by measuring the outgoing SEOS signal for different delays and knowing the incoming THz electric field. This approach can also be utilized to measure the emission of other THz sources to obtain their incoming electric fields. In our case, the THz source is the STE, and its THz field can be determined using MEOS. By keeping the probe pulse length and detection crystal constant, the system response remains unchanged. Therefore, by measuring the outgoing SEOS signal for other THz sources and multiplying it by the response function of the system, the incoming field can be determined. The theoretical evaluation of the response can be performed by reformulat-

ing the convolution in section (2.10) without an additional delay. Since the response of the system is real-valued, we can formulate the following relationship.

$$S(\omega) = \int \mathrm{d}t' \mathcal{F}_1 H^*(-\omega, t') E_{\mathrm{THz}}(t') \tag{56}$$

On this basis, we can evaluate this integral using Parseval's theorem, leading to

$$\tilde{S}(\omega) = \int \mathrm{d}\Omega \mathcal{F}_{12} H^*(-\omega, \Omega) \tilde{E}_{\mathrm{THz}}(\Omega) \tag{57}$$

On the other hand, the measured signal also can be expressed as

$$\tilde{S}(\omega) \propto \Delta E_{\mathrm{probe}}(\omega) E^*_{\mathrm{probe}}(\omega) C^* \tag{58}$$

For simplification, we can assume again as in equation (45) that the pump-induced change can be expressed as a convolution between the THz field and the probe field:

$$\tilde{S}(\omega) \propto E^*_{\mathrm{probe}}(\omega) C^* \int \mathrm{d}\Omega E_{\mathrm{probe}}(\omega - \Omega) E_{\mathrm{THz}}(\Omega) \tag{59}$$

By the comparison of this equation with equation (57), the response function can be identified:

$$\mathcal{F}_{12} H(\omega, \Omega) \propto C^* E^*_{\mathrm{probe}}(\omega) E_{\mathrm{probe}}(\omega + \Omega) \tag{60}$$

This result indicates that the transfer function results in zero if $\omega + \Omega$ reaches a value where the electric field of the probe is zero as well.

The response function for the more detailed modeling of the EOS can be

written as

$$\mathcal{F}_{12} H(\omega, \Omega) \propto 4\pi i \frac{\omega^2 t_{23}(\omega)}{c^2 k(\omega)} \chi^{(2)}(\omega - \Omega, \Omega) t_{12}(\omega - \Omega) t_{12}(\Omega) \frac{\exp(\mathrm{i}\Delta k d) - 1}{\Delta k}$$

$$C^* E^*_{\mathrm{probe}}(\omega) E_{\mathrm{probe}}(\omega + \Omega) \quad (61)$$

For the understanding of the SEOS response, we consider the simple model, since it contains the SEOS dynamics without the crystal response and showcases the dynamics of this methodology. For the modelling of the measured signals, the detailed modeling approach was taken.

2.11 Understanding the SEOS response

To better understand the response of our SEOS system (Figure 7), we assume that we can generate any THz electric field $E(t)$ by a superposition of δ-peaks according to the convolution

$$E(t) = \int \mathrm{d}\tau E(\tau) \delta_\tau(t) \tag{62}$$

The actual THz electric field in the lab is bandwidth-limited, depending on the bandwidth of the emitter. This THz electric field can be described as a convolution between a low-pass filter function H_{LP} and the general THz electric field:

$$E_{\mathrm{THz}}(t) = H_{\mathrm{LP}}(t) * E(t) \tag{63}$$

The low-pass filter function determines the bandwidth of the THz electric field since the emitted bandwidth is limited. With that the equation (62) can be written as

$$E_{\mathrm{THz}}(t) = \int \mathrm{d}\tau E(\tau) H_{\mathrm{LP}}(t) * \delta_\tau(t) \tag{64}$$

The convolution between the low-pass filter and the δ-pulse we define as D where the width is given by the bandwidth of the THz pulse. Thus, more narrowband THz pulses allow for longer peaks D. Therefore, to understand the signals delivered by SEOS, it is sufficient to understand the SEOS response to the peaks D. By taking the response function of our system $\mathcal{F}_1 H(\omega, t')$, we can evaluate the system's reaction to the peaks D for different delays:

$$\mathcal{F}_1 S(\omega, \tau) = \int dt' \mathcal{F}_1 H(\omega, t') D(t' - \tau) \tag{65}$$

The response function depends, as presented in Section (2.10), on the chirped probe pulse. For the modeling, we assume a Gaussian Fourier limited probe pulse with a pulse length of 50 fs which then gets temporally chirped to a pulse length of 1.2 ps. If the response function gets convoluted according to
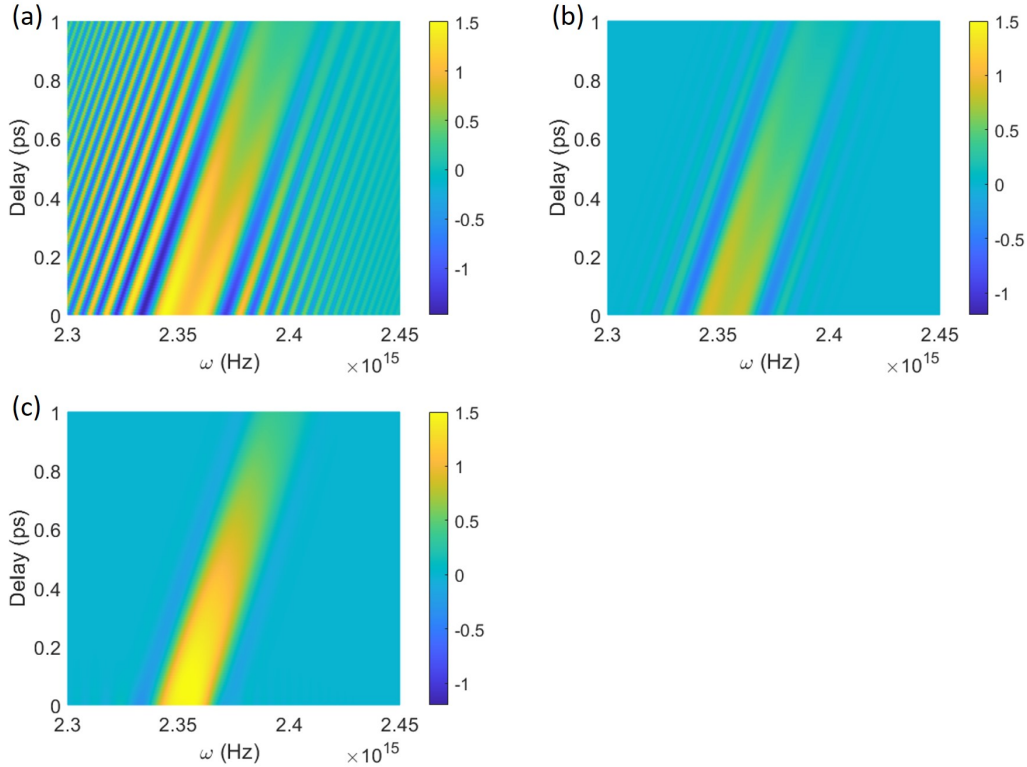

Figure 7 Signal $\mathcal{F}_1 S(\omega, \tau)$ for Gaussian pulses D shifted by the shown delays with a pulse width of 0 fs (a), 100 fs (b), and 200 fs (c).

equation (65) by a narrow peak with no pulse width, it acts like a δ-like pulse, and the resulting signal would reproduce the response function. By increasing

the pulse width of the incoming pulse to 100 fs, the resulting signal $\mathcal{F}_1 S(\omega, \tau)$ depicts a smeared-out version of the response function illustrated in Figure 7 (b). This signal showcases that the incoming Gaussian pulses can only be mapped onto the optical frequencies for this pulse width with some additional distortions. However, increasing the pulse width to 200 fs leads to a higher degree of smearing, which in turn reduces the level of distortions. As evident from the resulting signal depicted in Figure 7 (c), the incoming Gaussian pulse is mapped onto the optical frequencies in a clearer manner. This leads to the conclusion that the shorter the incoming pulse in time which is tantamount to larger bandwidth, the poorer is the mapping of the incoming signal onto the optical frequencies.

3 Experimental details

Over the course of this study, two distinct experimental setups were constructed to facilitate the execution of the MEOS and SEOS methodologies. Notably, each of these setups required a tailored approach to enable their successful implementation by the usage of a different character of the probe.
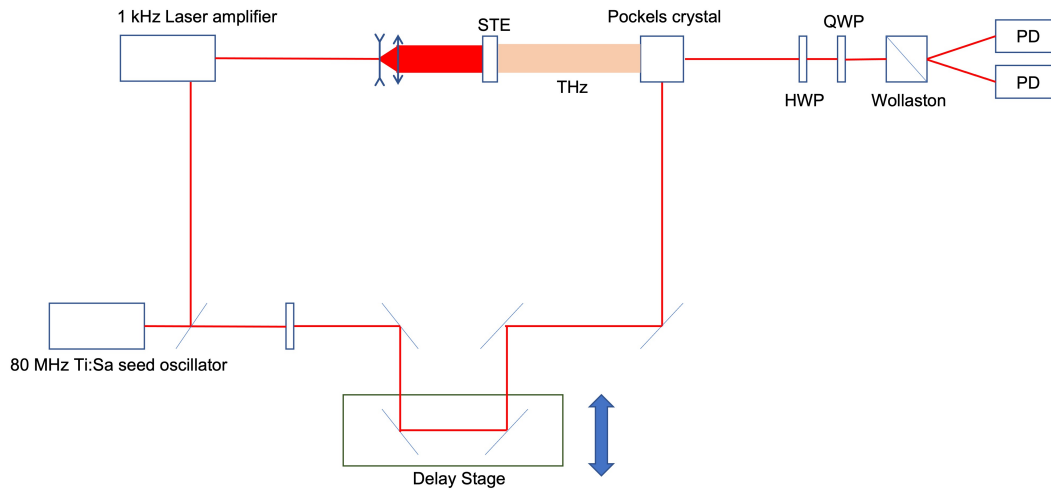
3.1 Multi-shot setup

Figure 8 The setup for the multi-shot electro-optic sampling with a Ti:Sa seed oscillator and 1 kHz regenerative amplifier.

For MEOS, two different lasers are used, where one laser acts as a pump and the other one as a probe. The pump pulse is generated by an amplified Ti: sapphire laser system (Coherent Legend Elite Duo) with a repetition rate of 1kHz and a center wavelength of 800nm. The energy contained in a single pulse can go up to approximately 5.7 mJ. The pump pulse goes through a telescope to increase the beam size. Afterward, it shines on the STE for the purpose of generating THz fields, which then hits the detection crystal. Two detection crystals were used, ZnTe and GaP. The ZnTe crystal had a thickness of 8 μm with a substrate with different crystal orientations afterward and the GaP had a thickness of 50 μm without a substrate. Inside the crystal, the THz pulse interacts with the probe pulse. The probe pulse is part of the laser system and is a seed oscillator with a repetition rate of 80 MHz and a center wavelength

of 800nm. The energy contained in one single pulse is approximately 0.2 nJ. Additionally, the probe pulse is connected to a delay stage, which alters the beam path to change the timing between the THz pulse and the probe pulse. In detection the p-polarized probe and the s-polarized THz interact with each other since a 0° or 90° angle between the polarizations of those two pulses is optimal [37]. Thereafter the now elliptically polarized probe passes a quarter-wave plate where its polarization changes into linearly polarized light again but with a slight tilt away from the initial p-polarization. The Wollaston prism splits it into two spatially separated components, which are measured by two balanced photodiodes.
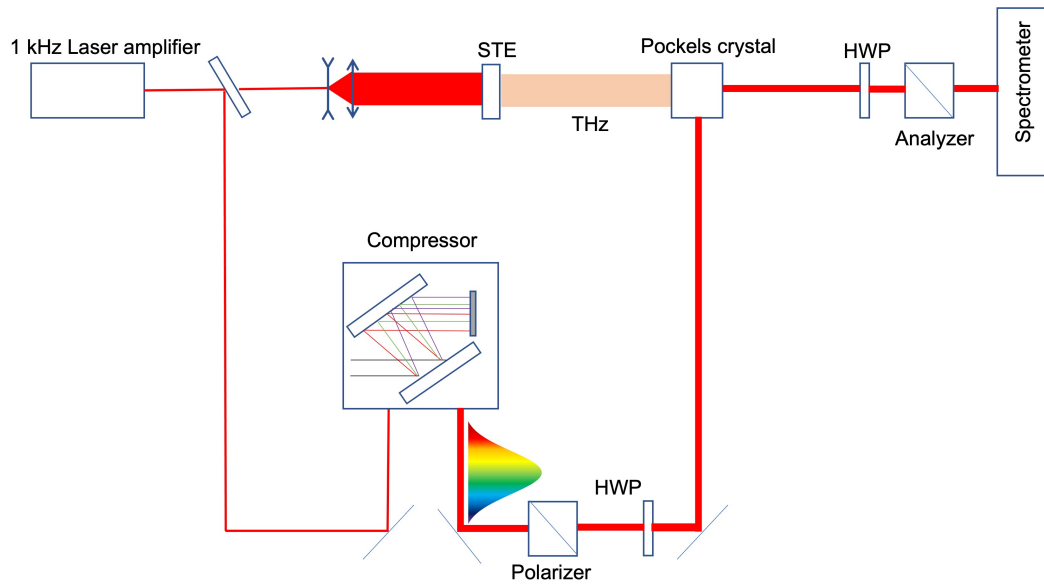
3.2   Single-shot setup

Figure 9 The setup for the single-shot electro-optic sampling with a compressor to chirp the probe pulse.

In the single-shot detection setup only the kHz laser, the same as in the multi-shot setup, are used. The laser is split into two components, where the stronger part goes again into a telescope and then STE to create the THz radiation. The minority part goes into a compressor, where the chirp pulse is generated. Afterward, a polarizer is placed to make sure, that the outgoing chirp pulse is linearly polarized. Then, a half-wave plate rotate the beam to achieve the 90°

difference between the probe and the THz. The quarter-wave plate transformes the ellipticity into a rotation. Afterward, the analyzer blocks the majority of the chirp pulse and lets the component through, which is generated by the interaction with the THz pulse. To optimize the signal, we minimized the signal from the chirp pulse with the QWP and the analyzer when only the chirp probe is hitting the spectrometer. After the THz induces a change in polarization, the initially fully minimized probe component gets less blocked by the analyzer, and therefore the overall signal, the THz on top of the probe signal, increases.

4 Experimental results

The current chapter is dedicated to the presentation of the measured signals obtained via both the MEOS and SEOS methodologies. In the case of the SEOS signal, the analysis commences with the raw signal acquired via the spectrometer, which is subsequently subjected to a frequency-to-time encoding process to obtain a time-dependent signal. This is then compared with the MEOS signal to enable a comprehensive comparative analysis of the two approaches. Finally, the measured SEOS signal is compared against a model signal derived from theoretical derivations, thereby giving an assessment of the efficacy and accuracy of the SEOS methodology in the context of THz detection. The insights gleaned from this analysis serve to enrich our understanding of the underlying principles and capabilities of the SEOS technique.

4.1 Multi-shot EOS

The common method to detect THz radiation in our lab is the multi-shot EOS. In Figure 10 (a) this technique was applied for 8μm ZnTe for two THz pulses generated by STE magnetized in opposite directions. The waveform has a duration of approximately 0.5 ps and is shaped like a single-cycle pulse with a flat beginning before and additional oscillations after the waveform. The oscillations are caused by resonances in the ZnTe detector crystal. The set-up was purged by nitrogen to omit absorption by water vapor. The flip of the external magnets caused a sign flip of the entire waveform. Additionally, the same procedure was performed for the GaP 50μm which shows the same behavior, when flipping the external magnetic field. Furthermore, the echoes of signals can be measured for GaP due to the absence of a substrate layer on top of it. The echoes for positive delay time with respect to the main waveform correspond to the probe pulse reflection and the ones for negative delay time to the THz pulse reflection. By Fourier transforming the MEOS signals in the time domain, its spectrum can be identified. Figure 10 (b) shows a bandwidth of approximately up to 10 THz for the $8\ \mu$m ZnTe. However, the response
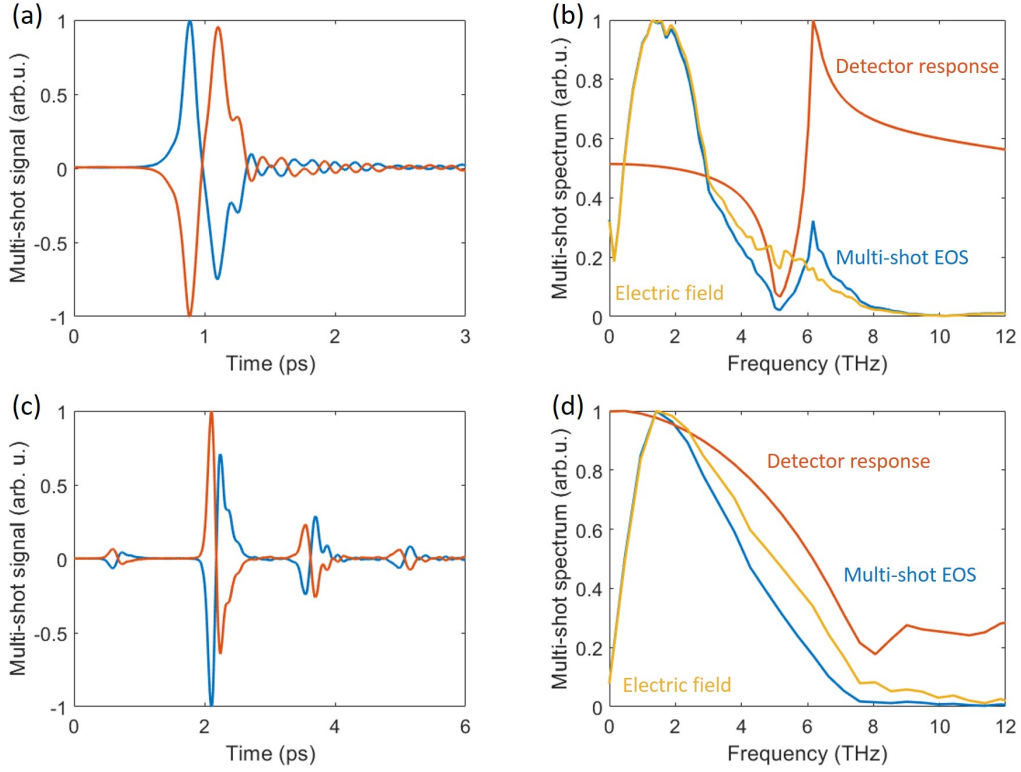
Figure 10 (MEOS measurement with a flip of external B-field for 8μm ZnTe (a) and $50~\mu$m GaP (b) using the STE of the THz generation. The spectral amplitude of MEOS signal, Detector response, and retrieved electric field for 8μm ZnTe (c) and $50~\mu$m GaP (d).

of the Pockels crystal influences the measured signal and, it is necessary to ascertain its frequency-dependent response. This detector response for 8 μm shows its prominent dip at the Reststrahlengap caused by a transverse optical phonon mode at 5 THz [38]. The multi-shot signal describes an LTI system and therefore can be described in the Fourier space as a multiplication between the THz pulse and the detector response $\tilde{H}_{\text{Det}}(\Omega)$:

$$\tilde{S}_{\text{EOS}}(\Omega) = \tilde{H}_{\text{Det}}(\Omega)\tilde{E}_{\text{THz}}(\Omega) \tag{66}$$

As a consequence, after the characterization and the simulation of the detector response [30; 33], the incoming THz electric field can be determined by a simple division in the frequency domain. This resulting retrieved signal can be used as the incoming field for modeling the single shot signal in the section (4.7). In the case of the 8 μm ZnTe, the phonon resonance at 5 THz and the non-

monotonic phase behavior disappear in the retrieval process. For the GaP, only the signal from 1.2 ps to 3 ps was considered, corresponding to the range for one single waveform without the echoes. This resulted in the spectrum, which only goes up to around 7 THz, originating from the thickness of the crystal since a higher thickness leads to a decrease in higher frequencies because of the increased velocity mismatch in thicker crystals. The resulting extracted signals for these two crystals should agree which is not the case.
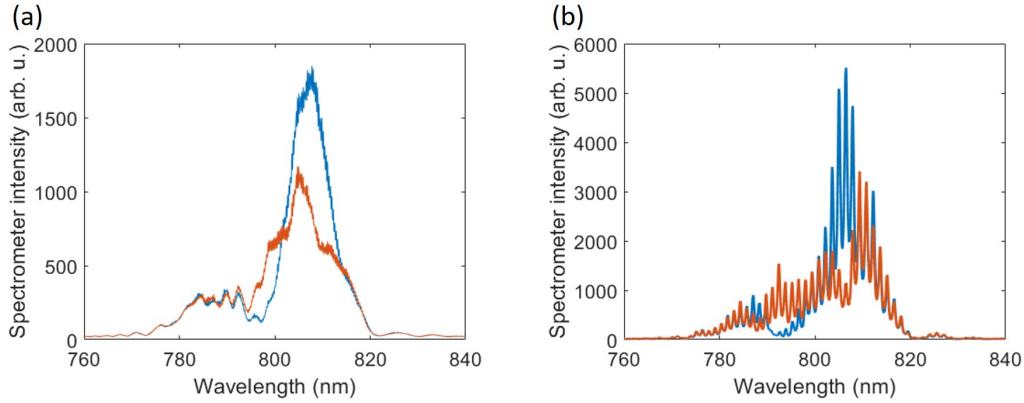
4.2   Raw data

Figure 11 Measured probe pulse after interaction with two opposing THz directions for 8μm ZnTe (a) and 50μm GaP (b)

As the first step of our analysis, we subtract the dark noise which is the impact of external influences like the ambient light when neither probe nor pump pulse is hitting the detector and therefore redundant spectral information. The probe pulse was directly focused into the spectrometer without using an optical fiber, to avoid absorption or non-linear effects in the fiber. Figure 11 (a) and (b) show the measured change in the spectrum when the THz pulse interacts with the probe pulse. The reversal of the THz pulse polarity was realized by changing the direction of the external field of the STE. As discussed in section (2.3) this leads to a change of the electric dipole and at the end a sign flip of the emitted THz electric field. For both detection crystals, the probe does not have a Gaussian-shaped signal. It is more of a blending of a smaller peak around 790 nm and a bigger one around 810 nm. For the 50 μm GaP, some

36

additional oscillations are visible. This is caused by echoes in GaP, same as in the MEOS measurement in figure 10 (c). Interference of a pulse $E_{\text{probe}}(t)$ with the same pulse, but a smaller amplitude and a time shift $aE_{\text{probe}}(t + \Delta t)$, lead to an oscillation following $a\cos(\omega\Delta t)$ in the frequency domain. The variables a and Δt describe a factor and a time shift, respectively. The first echo in the MEOS measurement appears after approximately 1.48 ps. This matches the period of around 1.4nm of the probe oscillations. For the evaluation of the single shot signal the following formula was used.

$$S_{\text{SEOS}} = \frac{S_{+\text{E}} - S_{-\text{E}}}{S_{+\text{E}} + S_{-\text{E}}} \tag{67}$$

The difference in the nominator was taken to retrieve the part, which increases linearly with E_{probe} and ΔE_{probe}. However, the same ellipticity appears smaller on the edge of the probe signal than at a position where the probe intensity is high. To compensate for that, the division by the sum of the signals for opposing THz orientations is taken. This is the quadratic contribution of E_{probe} and ΔE_{probe}, hence a normalization by the spectrum. This results in the following relationship:

$$S_{\text{SEOS}} \propto \frac{4\text{Re}(\Delta E_{\text{probe}}E_{\text{probe}}^*C^*)}{|E_{\text{probe}}|^2 + |\Delta E_{\text{probe}}|^2} \tag{68}$$

4.3   Frequency-to-time encoding

Frequency-to-time encoding represents a crucial step in the signal acquisition process, enabling the extraction of temporal information from spectrometer measurements. As discussed, the diffraction gratings generate a frequency-dependent phase shift, which can be leveraged to derive time-dependent signals from the raw spectrometer measurements. In the pursuance of the conversion from frequency to time, the single shot signal was determined for different timings between THz and probe pulse. The time shift is caused by moving a mirror and increasing the path of the pump beam before hitting the STE. Figure 12 (a) shows how through this increase in the path, the waveforms shift
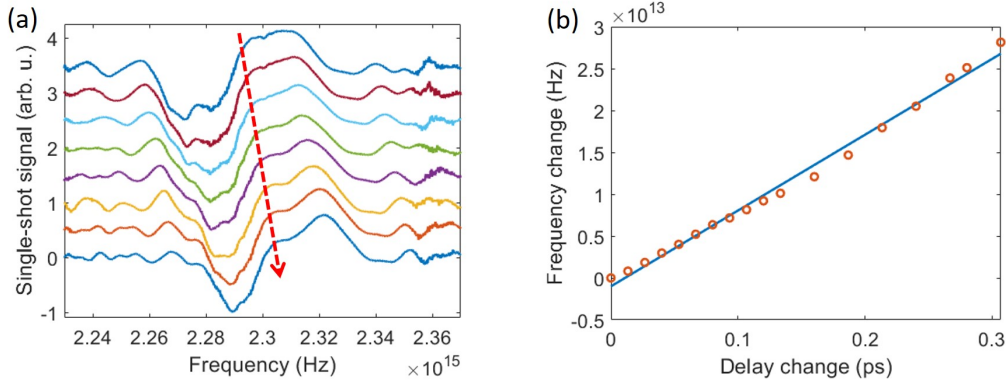
Figure 12 (a) SEOS signal for different timing between the probe and THz field. (b) Linear regression of delay change Δt and change in frequency $\Delta \omega$.

their positions in the spectrometer.

$$\tilde{S}_0(\omega) \Rightarrow \tilde{S}_1(\omega + \Delta\omega) \Rightarrow \tilde{S}_2(\omega + 2\Delta\omega) \tag{69}$$

Unfortunately, the waveform changes when shifting, because the system shown in Figure 12 (a) is not time-invariant. Therefore, it is inadequate to only determine how for example the maximum position shifts, when changing the light path, because it is not precisely assignable if the change of the maximum position is caused by the timing shift or by a change in the waveform. A better approach would be to investigate the dynamics in the Fourier domain. The signals can be described as

$$S_0 = A(\tau) \exp(i\phi_0) \tag{70}$$

$$S_1 = A(\tau) \exp(i\phi_0) \exp(-i\Delta\omega\tau) \tag{71}$$

The $\Delta\omega$ is then a phase shift in the Fourier domain. These signals can then be multiplied by each other and yield

$$h_1(\tau) = \tilde{S}_0 \tilde{S}_1^{\,*} = |A(\tau)|^2 \exp(-i\Delta\omega_1\tau) \tag{72}$$

38

The result contains the frequency shift $\Delta\omega_1$ from the signal S_0 to S_1. The weighted average of the frequency shift $\Delta\omega$ is expressed by

$$\Delta\omega = \frac{\sum_\tau |h_n(\tau)|\Delta\omega_n\tau}{\sum_\tau |h(\tau)|\tau^2} \tag{73}$$

Here, we define frequency shifts with respect to the first signal $\tilde{S}_0$. Figure 12 (b) shows the frequency shift $\Delta\omega$ in relation to the change in delay Δt. The dependence points to a linear relationship, thus a linear regression can be performed which indicates, that the chirp is linear, and conversion from Hz to ps can be performed by determining the slope of the fitted line:

$$\Delta\omega = m\Delta t \tag{74}$$

with m being slope. The frequency-to-time encoding was performed for the 8 μm ZnTe crystal and as the probe pulse was kept constant, the encoding would yield the same result for the 50 μm GaP. The slope of the fitted line was $9.052 \cdot 10^{25} \; \frac{\text{Hz}}{\text{s}}$.

4.4 Single Shot measurement

After the frequency-to-time encoding, the measured signal on the spectrometer can be translated to a signal in time. This makes a comparison to multi-shot EOS possible, as seen in Figure 13. Figure 13 (a) shows that the single cycle of the SEOS signal is slightly longer than the MEOS one, which is explainable through the distortions of the single-shot, explained in Section (2.7). Since in our case, we chose a probe pulse length, which approximately covers the THz waveform, it leads only to small smearing of the single shot signal. The bandwidth of the SEOS for ZnTe is slightly smaller than the MEOS method and we are not able to detect the higher frequencies up to 10 THz. The achieved single-shot detection bandwidth reaches 7 THz and 8 THz for 8 μm ZnTe and 50 μm GaP, respectively. This is higher than the published papers with this methodology [16] [39], reaching only 3 THz. The feature associated
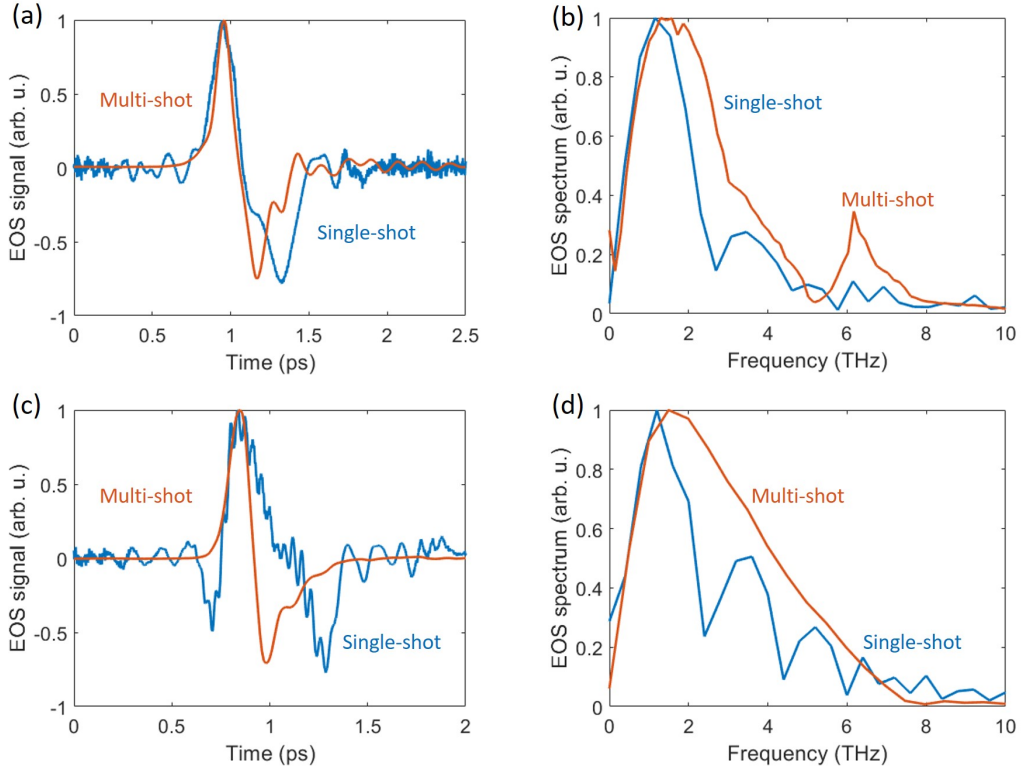
Figure 13 Comparison between the MEOS and SEOS signal in the time domain for $8\,\mu$m ZnTe (a) and 50 μm GaP (b). Comparison between the MEOS and SEOS signal in the frequency domain for $8\,\mu$m ZnTe (c) and 50 μm GaP (d).

with the Restrahlengap at 5 THz for ZnTe appears to move its position. It is important to note that the resolution of the spectrum of SEOS is low. This is caused by the chosen time window for the Fourier transformation of the signal. The window is limited by the probe pulse length which is limited by the THz pulse duration. Thus, we will always have a low resolution in the spectrum since the dynamics of the probe pulse only goes up to 2.5 ps. The 50 μm GaP has some additional oscillations caused by the reflection of the echoes. Since the interference leads to a multiplication of the probe pulse with $a\cos(\omega\Delta t)$, the cosine term remains in the nominator in equation (67) and appears as an oscillation in the signal. This oscillation measured by the spectrometer will also be translated into time information. In the spectrometer, they had a period of roughly 1.4 nm which translates with the frequency-to-time conversion to a period of 0.05 ps in time. That in turn has a frequency of 20 THz. Since in our detection method, we only measure up to 8 THz, the oscillations in

the time domain will not affect the part of the spectrum of interest. The interference is independent of the chirp and always appears as interference in the spectrometer. They do not appear for the ZnTe crystal, because there a substrate is used to avoid a strong change in refractive index and therefore the echoes. We conclude that the oscillations of the signal in time are only caused by the usage of a spectrometer, not by the chirp or the THz pulse. In Figure 13 (c) the distortions in the time domain appear to be stronger in the case of GaP compared to the ZnTe since it showcases a stronger single-cycle broadening in the single-shot measurement. Additionally, a strong pre-oscillation is detectable. In figure 13 (d) the spectrum of the GaP 50 μm is illustrated. The bandwidth of the SEOS appears to be similar to the MEOS and goes up to 8 THz. The SEOS spectrum has additional fringes in the spectrum which are presumably caused by the chirp.
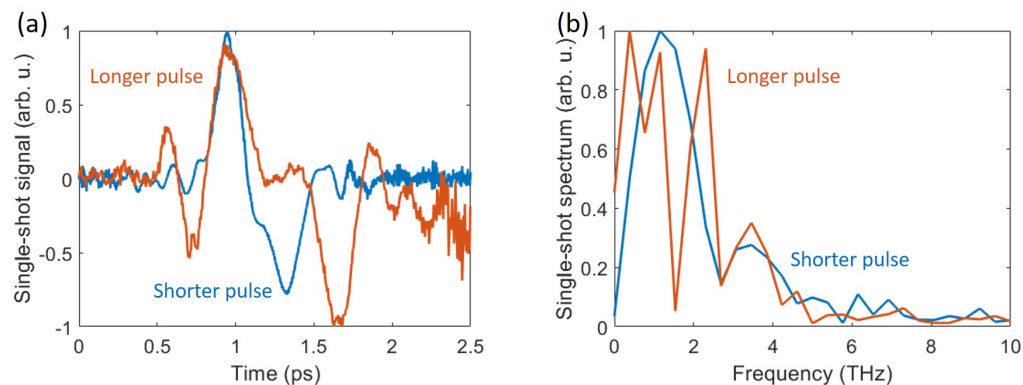
4.5 SEOS for a different pulse length

Figure 14 (a) SEOS signal for different probe pulse lengths in the time domain. (b) SEOS signal for different probe pulse lengths in the frequency domain.

In SEOS, commonly discussed distortions are evident in Figure 14. The considerably longer single cycle and higher amplitude in oscillations before and after the single cycle are vehemently noticeable. The employed increase in GDD is approximately 3.6-fold, which would translate to a probe pulse duration that is roughly twice as long. The noisy character in the time domain is due to a shorter amount of averages taken compared to the signal with

a shorter probe pulse. The spectrum shows, for the longer probe pulse an appearance of strong oscillations, particularly for smaller THz frequencies. It is crucial to note that a longer pulse in time means a shorter coverage of the signal on the spectrometer, resulting in fewer sample points for the signal in the time domain and leading to a lower resolution in the spectrum.

4.6 Chirp pulse length

The determination of the pulse length of the chirp pulse is a crucial step for modeling the signal. Depending on the pulse length, the resulting signal can change in its dynamics. On the spectrometer, the pulse length can be determined with the help of the equation (24) and by identifying the width in the frequency domain. But the phase gets lost due to the fact that the spectrometer takes the absolute square of the incoming electric field. Therefore, with the frequency-to-time calibration in the section (4.3), we can identify the pulse length of the chirp probe pulse. In the experiment, the distance between the
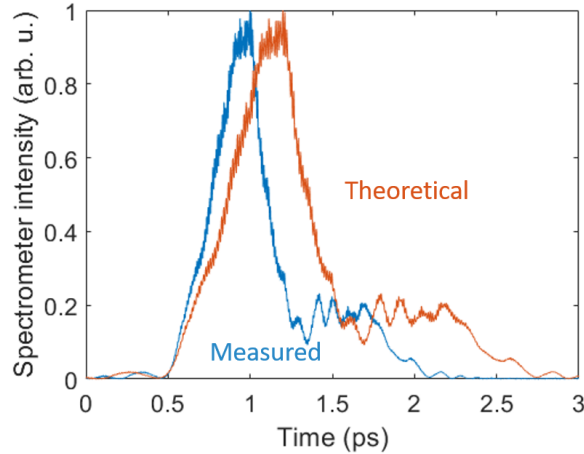

Figure 15 Comparison between the pulse length determined by the experimental and theoretical frequency-to-time conversion.

transmission gratings was chosen to be 9cm with an angle of incidence of a few degrees. They had a periodicity of 300 lines per mm. Combining all the variables, the GDD could be calculated, and the laser chirp rate for the theoretical frequency to time conversion using equation (47) as well. The initial pulse length τ_0 before going into the compressor was measured using spectral

Phase Interferometry for direct electric-field reconstruction (SPIDER). The initial pulse can not be defined by the pulse measured with the spectrometer since it is not fourier-limited due to a large amount of dispersive optics. Figure 15 shows the comparison between the theoretical and experimental determined pulse length. The theoretical one shows an approximately 1.3 times longer pulse.

4.7 Single-shot Modelling

For the modeling of the pump-induced change, equation (48) was used. Here, for the incoming THz electric field, the measured MEOS signal was taken and deconvoluted according to equation (66), and the retrieved electric field was taken. For the probe electric field, the measured probe signal on the spec-
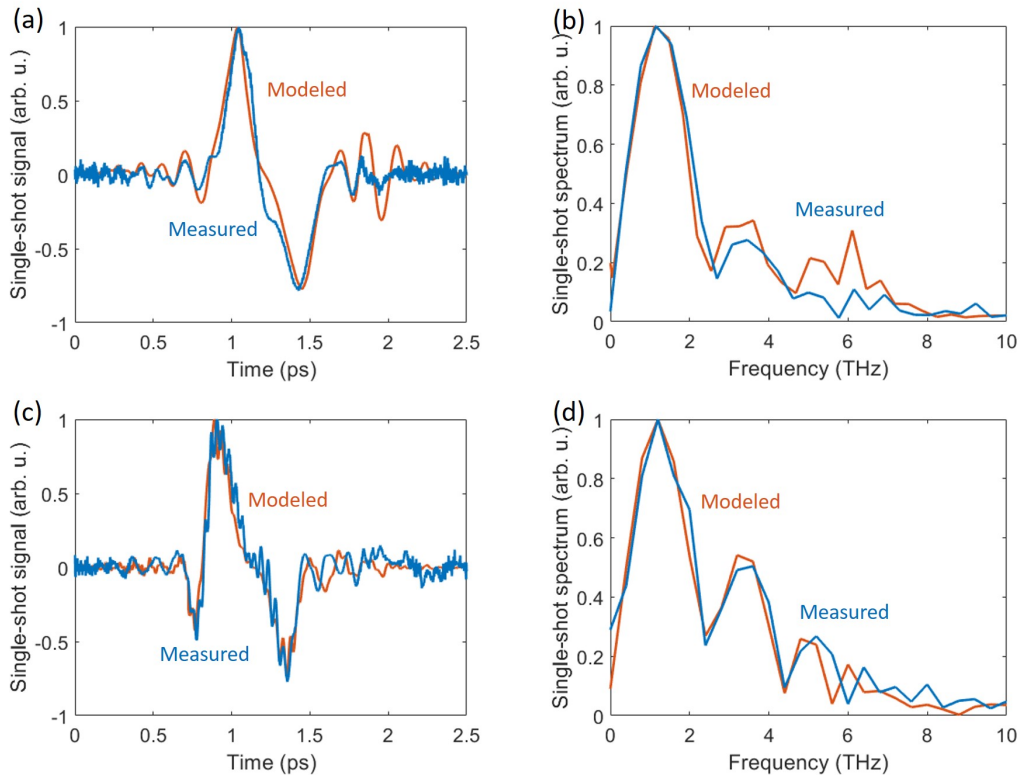

Figure 16 Comparison of the MEOS and SEOS signal in the time domain for 8 μm ZnTe (a) and 50 μm GaP (b). Comparison of the MEOS and SEOS signal in the frequency domain for 8 μm ZnTe (c) and 50 μm GaP (d).

trometer was chosen, whereby the phase needed to be calculated. The previous chapter showed us, that there is a slight disagreement between the theoretical

and experimental chirp calculations. Therefore, the GDD value was retrieved from the measured frequency-to-time encoding. A good indicator for proper matching is if the oscillations of the signals in time are matching. Because the measured signal is proportional to the probe electric field E_{probe}, where the oscillations come from. If the oscillations in the time domain match, the GDD and therefore the chirp is fitting. Figure 16 (a) shows for the ZnTe a good agreement between the measured and modeled signal. The overall dynamics are comparable, but the modeled signal shows stronger features in the oscillations. For example, after the waveform, there are some strong oscillations in the modeled signal which do not appear in the measured one. The model for the GaP displays some disparities in the phase of the oscillations, but the overall waveform could be replicated. For the spectral information, both time traces were Fourier transformed from 0 to 2.5 ps, identical to the measured signal. Both spectra exhibit discrepancies in the minima of the oscillations. In the ZnTe the first minimum shows a slight mismatch in the first minimum and stronger features afterward. In the GaP the first two oscillations match, but the third minimum also comes 0.1 THz prematurely, and the maximum afterward as well.

Moreover, in the modeling, the dynamics after the crystal are not taken into account. That means the change in pulse shape through the polarizer and QWP before hitting the spectrometer. Furthermore, the spectrometer response was not considered. These factors can influence the shape of the modeled signal.

5 Discussion

The present chapter aims to provide a discussion of the limitations of the SEOS methodology. To this end, the relative dynamics change of two different detection crystals used in the SEOS methodology is also evaluated and the reasoning for a difference in measurement results is presented. Finally, suggestions for the improvement of the methodology are proposed.

5.1 Limitations of SEOS

In this work, we built a single-shot detection setup to perform an EOS measurement. A comparison with the MEOS method enables us to recognize its strengths and weaknesses. The MEOS allows us to detect THz frequencies up to 10 THz and 7 THz for 8μm ZnTe and 50 μm Gap, respectively. Generally, using the STE, an emission of up to 30 THz can be achieved [19]. The STE emission is fourier-limited and depends on the pump pulse length [19]. The detected bandwidth is by a factor of 3 smaller, therefore the incoming pump pulse could be chirped by the optical elements in usage before generating the THz field. The SEOS shows frequencies up to 7 THz for the ZnTe and 8 THz for the GaP. Above 10 THz the spectrum indicates some amplitudes, but this is presumably produced by the noise. Considering that in the frequency-to-time conversion from the spectrometer signal, the noise will also be converted. By making the chirp probe pulse shorter, we should improve the bandwidth. Certainly, the probe pulse should be longer than the incoming THz signal, otherwise, the dynamics will not be detected. This showcases the major limit of single-shot detection. If the duration of the emitted source is unknown, the chosen probe pulse length could distort the emitted THz signal. This was shown by the choice of longer probe pulse length, where the distortions are so profound, that the higher frequencies are not detectable anymore. Therefore, for an unknown source, the probe pulse has to be changed, to optimize the bandwidth of the detection.

5.2 Probe pulse duration

The comparative analysis of the theoretical and experimental calculation of pulse duration has produced disparate results. One possible explanation for this disparity is that the measured probe pulse may not adhere to a Gaussian distribution, causing the application of equation (47) inaccurate in converting frequency to time using the laser chirp rate. The distortion in the shape of the probe pulse could arise due to absorption by various mirrors and optical components. Additionally, post-chirping, a polarizer, HWP, and filters were employed, which could introduce a positive dispersion effect, and counteract the negative dispersion introduced by the compressor, thereby causing a slight reduction in the chirp pulse length and ultimately leading to a shorter measured pulse, which concurs with the measurement. Furthermore, variables that impact chirp or GDD may not be accurately determinable, such as the beam's angle of incidence and center frequency. Another argument to consider is the potential non-linearity of the chirp, which could be attributed to a third-order term in the Taylor expansion of the phase. However, for the distance chosen, the third-order term with a magnitude of 10^{-11} fs^2 is considerably lower than the GDD value around -1100 fs^2, indicating that assuming linearity in the chirp is a fitting assumption

5.3 SEOS with GaP and ZnTe

The experimental results obtained from using two different detection crystals in the SEOS showed significant differences. Notably, the SEOS of GaP demonstrated a proportionally longer single cycle compared to that of ZnTe, with a strong pre-oscillation before the single cycle. The measurement of the ZnTe crystal with a longer probe pulse exhibited similar behavior, indicating that the GaP crystal interacted with a significantly longer probe pulse. However, since all variables that could influence the GDD were kept constant, this observation was unexpected. Consistent with the modeled result, both the change in waveform and the modulation in the spectrum of GaP could be replicated and
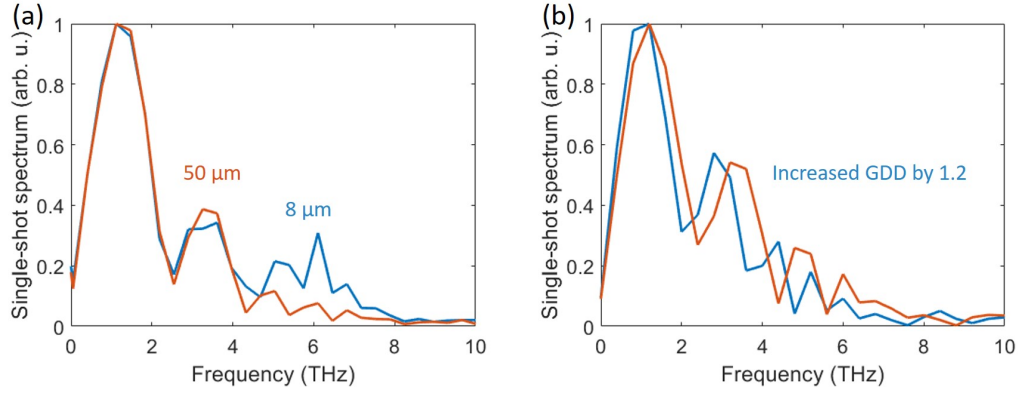
Figure 17 (a) Modeled single-shot spectrum for ZnTe for a thickness of 8 μm and 50 μm. (b) Modeled single-shot spectrum for GaP for different GDD factor.

therefore have to be induced by the additional substrate, the thickness, or the detection crystal itself. We can rule out the additional substrate as a potential source of signal distortion since back reflection inside the GaP only causes fringes in the time domain. These oscillations only contribute to a frequency range that is not of our interest. Additionally, the thickness of the substrate in the order of micrometers is too small to induce additional dispersion. However, the thickness of the crystal can lead to phase-matching oscillation due to a mismatch in the wave number, which can result in a strong oscillation in the electric field component of the pump-induced change. This can lead to a distortion in the SEOS signal in both time and spectrum domains. Therefore, the thicker the crystal, the stronger the distortion in the SEOS signal. To confirm this hypothesis, we could measure the ZnTe crystal with a thickness of 50 μm and examine the change in dynamics and the influence of the phase-matching condition. Nevertheless, a change in the thickness in the modeling did not lead to a drastic change in signal severity at 50 μm between the two materials. In Figure 17 (a) the spectrum for increased thickness to 50 μm in the modeling could not replicate the prominent oscillation in the GaP. Finally, the SEOS signal is highly dependent on the crystal response, which is likely the most significant origin of differences in the resulting waveform and spectrum. The observed strong modulation in GaP in the spectrum is likely induced by the chirp of the probe, as changing the GDD parameter results in a shift in

47

the modulation positions. But it is expected that, even if the modulation is less apparent in ZnTe, the periodicity should remain the same since the probe pulse length is constant. However, when comparing the two detection crystals using the MEOS method, they exhibit different frequency-dependent behaviors. GaP showed a monotonic falling dependence from around 2.2 THz with an approximately constant slope. When multiplied by an oscillation, it would result in an oscillation with a decreasing envelope. Moreover, the ZnTe does not show this monotonic behavior and is strongly influenced by the Restrahlengap at 5 THz. Multiplying this behavior with an oscillation would lead to a significantly different result and could explain why this oscillation is not that apparent in the ZnTe measured with the SEOS method. To investigate the theory that the fringes are caused by the chirp of the probe pulse, the GaP was modeled for a different probe pulse length. Upon increasing the GDD factor in the modeling of the GaP crystal by a factor of 1.2, the minima of the fringes in the spectrum exhibited a shift, as depicted in Figure 17 (b). The observed shift in the fringes towards the earlier part of the spectrum is consistent with the fact that longer probe pulses result in longer single cycles of the signal in the time domain. In the case of the measurement with a longer probe pulse with the ZnTe crystal, pronounced modulations were detected even earlier in the spectrum compared to the model in Figure 17 (b) due to the higher GDD factor of 3.6. These modulations appeared in the 1-5 THz range as this range was not affected by the Restrahlen dip, and thus, allowed for their detection in the ZnTe crystal compared to the measurement with the shorter probe pulse. To conclude, the measurements indicate that when measuring with SEOS, the signal will contain a modulation in the spectrum caused by the chirp of the probe. The slight incongruities between the modeled and measured signals have to be discussed. The primary root cause for these inconsistencies can be attributed to the underlying assumptions made regarding the incoming THz signal. The incoming Thz signal was computed by using the MEOS signal, deconvoluted by the detector response. The outcomes obtained for both crystals displayed notable deviations from the anticipated THz signal. Figures 18
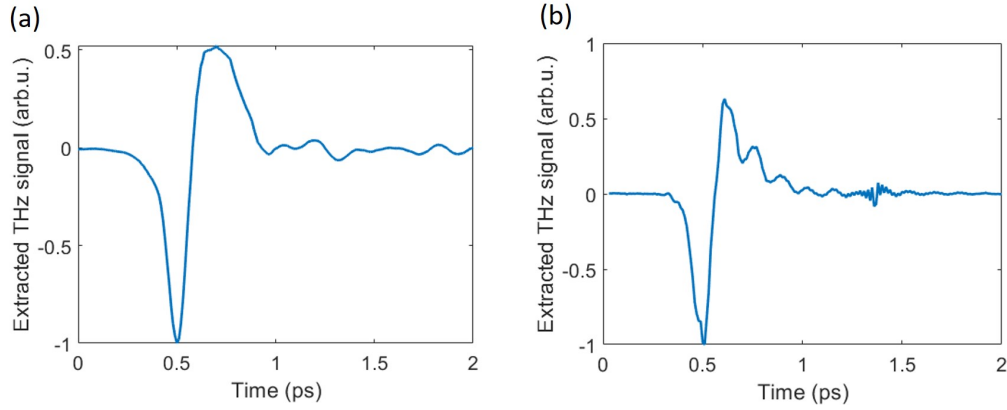
48

Figure 18 Extracted THz signal for 8 μm ZnTe (a) and 50 μm GaP (b).

(a) and (b) illustrate the extracted THz signal for ZnTe thicknesses of $8\mu m$ and $50\mu m$ GaP, respectively. These signals display a single-cycle waveform with additional oscillations, suggesting the presence of residual dynamics arising from crystal response and water vapor. However, it should be noted that this behavior is incorrect since the emitted THz beam from the STE does not contain both. To gain a more accurate description of the incoming THz field, one would need a better determination of the driving field. Another significant source of error in the modeling process is the probe's electric field. Although the measured probe signal on the spectrometer is utilized in the analysis, its shape may change after interacting with the detector crystal and subsequently measured in the spectrometer. A more precise evaluation would involve measuring the probe field immediately after the ZnTe crystal.

5.4 Improvements

Multiple improvements can be utilized to make the SEOS methodology a more valuable tool. The single-to-noise ratio can be enhanced by using two spectrometers. The measurements in this work were performed by switching the external field and causing a sign flip in the emitted THz field from the STE. This was done to retrieve the linear component of the probe and the pump-induced change $S_{\text{SEOS}} \propto \Delta E_{\text{probe}} E_{\text{probe}}^* C^*$. On the other hand, this could be achieved by changing using a Wollaston as seen in Figure 19.
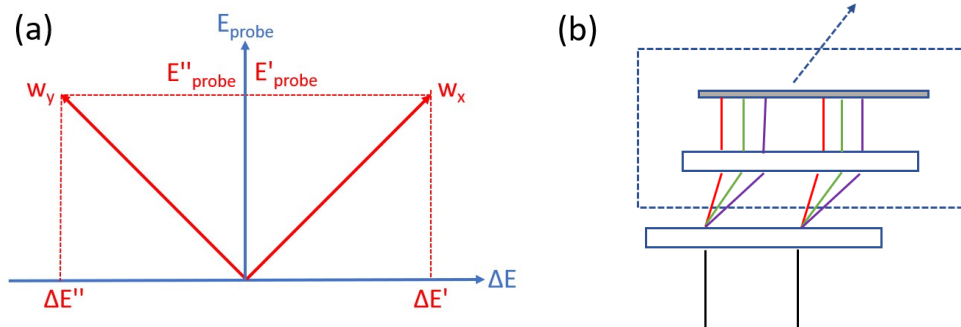
Figure 19 (a) Projection of E_{probe} and ΔE_{probe}, when using a Wollaston prism. (b) Transmission grating setup when using a delay stage.

In this geometry, the x-axis represents the pump-induced change ΔE_{probe} and the y-axis the probe field E_{probe}. The Wollaston prism is set up in a way, that the w_x and w_y have a 45° and 135° angle to the x-axis, respectively. These are the s- and p- components emitted by the Wollaston prism. They both have two projections to each axis, whereby $E'_{probe} = E''_{probe}$ and $\Delta E'_{probe} = -\Delta E''_{probe}$. This would mean, that with one shot, all the necessary measurements can be done to obtain the signal since a one-shot measurement would measure the positive and negative pump-induced components. If you detect both signals from the Wollaston, you can subtract them and acquire the linear part as before. In this work, we still require two shots for the detection of a waveform, while using a Wollaston could improve the signal-to-noise ratio because only performing one shot would avoid distortion from one to the next. Additionally, this also would reduce the acquisition time. The downside of using this Wollaston is, that in reality, E_{probe} is significantly stronger than ΔE_{probe} component. This means a spectrometer with a large dynamic range is necessary, which handles the probe's electric field without saturating and simultaneously measures a small change in intensity caused by ΔE_{probe}. Otherwise, the E_{probe} has to be reduced remarkably by the usage of filters or polarizers.

An additional improvement that could be implemented is the construction of a stage that facilitates more effortless modification of the distance between the gratings. In our current configuration, the reflection or transmission gratings are attached to fixed posts, necessitating the dismounting of components to ad-

just the distance. Ideally, the second grating along with the mirrors should be mounted on a movable stage that moves in tandem with the diffraction angle of the first grating. This would simplify the alteration of the chirp length.

6 Conclusion and outlook

In this work, the development of an SEOS setup was realized and proved to be a valuable technique for detecting broadband THz signals. Our SEOS technique allowed us to successfully measure broadband THz pulses up to a frequency of approximately 7 THz and 8 THz using the 8 μm ZnTe and 50 μm GaP, respectively. With that, we outperformed the highest published bandwidth of approximately 3 THz. Additionally, our findings demonstrated that the SEOS methodology induces a modulation in the spectrum of the measured signal. We also showed that the degree of modulation depends strongly on the duration of the probe pulse. Finally, we were able to achieve successful modeling of our measurements through a more detailed approach that involved accounting for the crystal response and phase-matching condition in the interaction between the THz and probe pulse. This approach allowed for a deeper understanding of the underlying dynamics of the system. By experimentally determining the response function, we can further extend our ability to evaluate the incoming THz field for materials with relatively low THz emission amplitudes. For that, we have to vary the delay between the THz pulse and the chirp probe pulse. In this work, we only varied the delay up to 0.3 ps, thus would lead to a low resolution after Fourier transformation. For future plans, we can vary the delay further and also determine the two-dimensional response function experimentally as well, since the method for calculation has already been demonstrated.
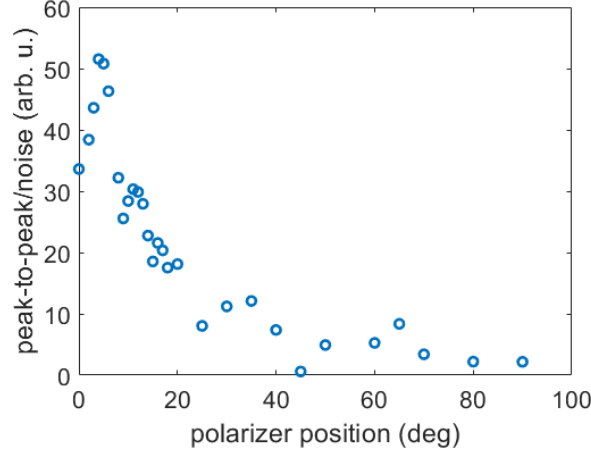
A Appendix

A.1 Polarizer dependence

Figure 20 Peak-to-peak divided by the noise for different polarizer positions.

By changing the polarizer position, the contribution of the probe field to the SEOS signal can be changed. When aligning the blocking axis of the polarizer exactly parallel to the probe's electric field, it blocks the field fully. Theoretically, it should result in no SEOS signal because E_{probe} is zero. In reality, there is still some contribution from E_{probe} since the polarizer does not fully block. By increasing the angle from the parallel position, the contribution of E_{probe} increases, and $\Delta E_{\mathrm{probe}}$ decreases. At 90 degrees there should be no contribution from $\Delta E_{\mathrm{probe}}$ and maximized contribution from E_{probe}. The goal was to find the polarizer position where the signal-to-noise ratio is the highest. For that, we varied the angle for the polarizer and investigated the signal using the following formula.

$$\text{Signal-to-noise ratio} = \frac{\max(S_{\mathrm{SEOS}}) - \min(S_{\mathrm{SEOS}})}{\sigma(S_{\mathrm{SEOS,Noise}})} \tag{75}$$

Here, the peak-to-peak was calculated by subtracting the maximum value from the minimum, and the noise by calculating the standard deviation σ for the region where no signal was detected. Figure (20) shows that at already 5 and 6 degrees, the Signal-to-noise ratio maximizes. This means only a small

contribution to the E_{probe} is necessary. The setting at 6 degrees was chosen for the SEOS measurements.

A.2 Longer probe pulse

The technique of frequency-to-time encoding was applied to the longer probe pulse using the same methodology as for the shorter one. By analyzing the measured probe field on the spectrometer, the wavelength was converted into a time signal which enabled the determination of the probe pulse length in time. The resulting probe signal for the longer probe pulse exhibited an approximately two-fold increase in pulse length. However, the signal displayed different shapes which could be attributed to chirping effects, as well as possible differences in alignment since the signals were measured months apart.
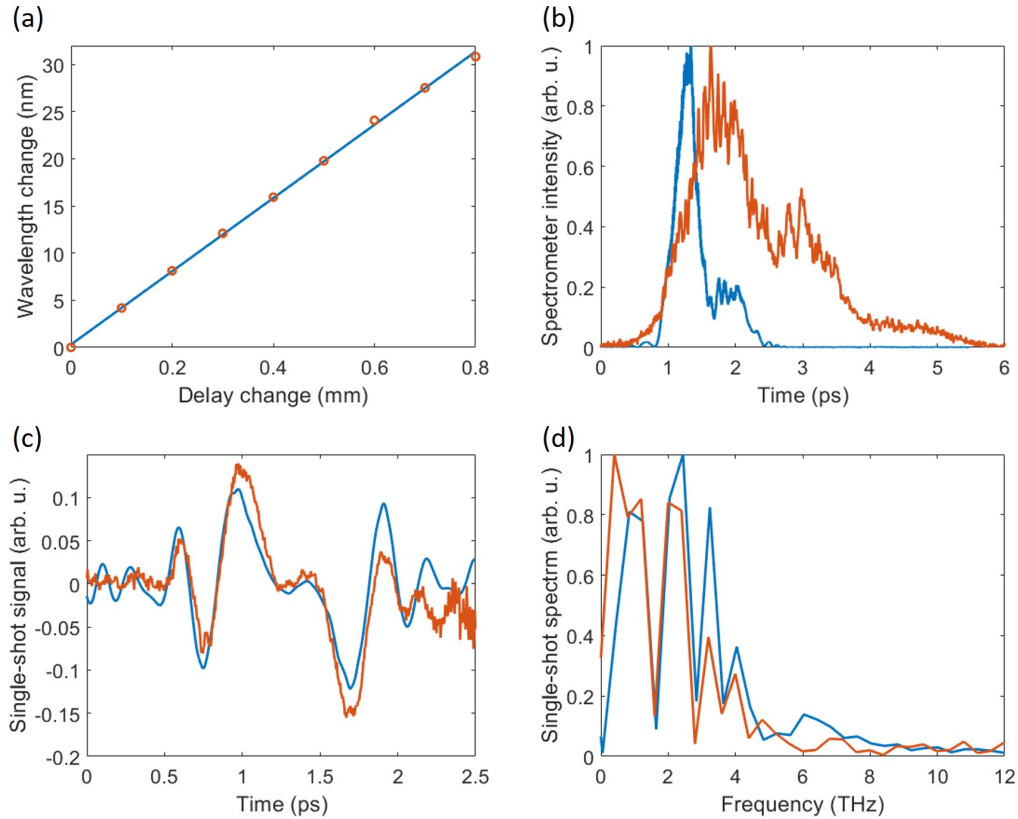

Figure 21 (a) Linear regression of delay change Δd and change in wavelength $\Delta \lambda$ (b) Pulse length comparison of the probe pulse using the frequency-to-time encoding (c) Modeled signal in the time domain (d) Modeled signal in the frequency domain.

In terms of modeling, good agreement was observed for the longer pulse,

with the single cycle and two additional oscillations being accurately replicated. The spectrum investigation exhibited a notable modulation in the lower frequency range, which signifies that the extended pulse duration led to oscillations in the lower frequencies. The underlying reason for this phenomenon is the temporal spreading of the waveform, which amplifies as the probe pulse length increases, resulting in a modulation in the spectrum. This observation confirms the idea that the modulation was not visible for the short pulse length due to the crystal response, which has a better-behaved crystal response in the 1-4 THz frequency range. Hence, the modulation can be detected in this frequency range.
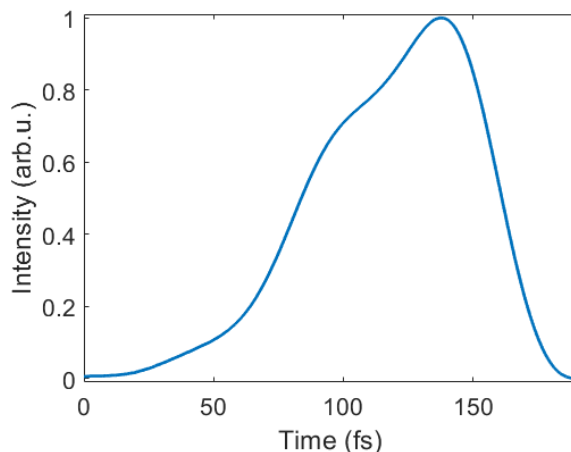
A.3   SPIDER measurement

Figure 22 The measured intensity with SPIDER

The intensity measured using SPIDER is presented in Figure (22), where the probe pulse was measured before going into the compressor where it got broadened. The shape is not Gaussian similar to the probe electric field measured on the spectrometer in the SEOS measurements. But it looks closer to a Gaussian-shaped beam. This led to the conclusion, that either the compressor or the optical elements afterward could cause a further change in shape. The pulse width was measured to be approximately 75 fs, which is longer than the Fourier-limited pulse width of approximately 40 fs. Thus, the pulse arriving

at the STE likely contains a pulse that can be shortened to achieve a higher bandwidth in the emitted THz electric field from the STE. To perform the theoretical conversion from wavelength to time using equation (47), the initial pulse length of 75 fs was used.

B   List of abbreviations

DFG Difference-frequency generation

EOS Electro-optic sampling

FM Ferromagnetic

GaP Galium Phosphite

GDD Group delay dispersion

GVD Group velocity dispersion

ISHE Inverse spin Hall effect

LTI Linear time-invariant

MEOS Multi-shot electro-optic sampling

NM Non-magnetic

SEOS Single-shot electro-optic sampling

SFG Sum-frequency generation

STE Sprintonic Terahertz emitter

SPIDER Spectral Phase Interferometry for Direct Electric-field Reconstruction

THz Terahertz

Ti:sapphire Titanium-doped sapphire crystal

ZnTe Zinc Telluride

C Acknowledgment

I really want to use the opportunity to thank the people who supported me during this project.

Tobias Kampfrath who I deeply esteem not only as a scientist and teacher and as a human for his humble and friendly way.

Christian Frischkorn for being my second supervisor and organizing a wonderful conference where I could participate.

Alexander Chekhov who helped me and answered my questions regardless of being busy or having time constraints.

Bruno Serrano who supported me immensely at the beginning of the project. Also, the amazing and funny time during our studies and being such a fantastic friend.

Yannic Behovits for being a big help in the lab and outside of the lab since he always had some creative and smart ideas.

I also want to express my gratitude to the rest of the THz group. Everybody created such a wonderful atmosphere on a professional and personal level.

Anton Klimek as a fellow student and a wonderful friend who always had some creative and interesting perspective on physics.

My partner Clara for her support, love, and making every day more wonderful and beautiful.

My sister Mona for always being at my side, being my anchor, and for the interesting discussion I can have with her.

Of course my parents Kayoko and Peter for their support and love. I always felt encouraged and supported in the way I am and how I pursue things.

All the close people and friends in my life for making life so fun and beautiful.

References

[1] **Yun-Shik Lee** Principles of Terahertz Science and Technology, Springer (2009)

[2] **T. Kampfrath, A. Sell et al** Coherent terahertz control of antiferromagnetic spin waves, Nature Photonics 5(1), 31–34 (2011).

[3] **S. L. Dexheimer** Terahertz spectroscopy: principles and applications, CRC press (2017)

[4] **T.Kampfrath, L.Perfetti et al** Strongly Coupled Optical Phonons in the Ultrafast Dynamics of the Electronic Energy and Current Relaxation in Graphite,Phys. Rev. Lett. 95, 187403 (2005)

[5] **S. Leinss, T. Kampfrath et al** Terahertz Coherent Control of Optically Dark Paraexcitons in Cu_2O, Physical Review Letters 101(24), 246401 (2008)

[6] **W. Zhang, P. Maldonado et al** Study of Ultrafast Magnetism by THz Emission Spectroscopy. 44th International Conference on Infrared, Millimeter, and Terahertz Waves (IRMMW-THz) (2019)

[7] **E. Isgandarov, X. Ropagnol et al** Intense terahertz generation from photoconductive antennas, Frontiers of Optoelectronics 14, 64-93 (2021)

[8] **A.Sign,A. Pashkin et al** Gapless broadband terahertz emission from a germanium photoconductive emitter, ACS Photonics 5, 2718 (2018)

[9] **H. Zhao, Y. Tan et al** Efficient broadband terahertz generation from organic crystal BNA using near infrared pump, Applied Physics Letters 114, 241101 (2019)

[10] **H. Hirori, A. Doi** Single-cycle terahertz pulses with amplitudes exceeding 1 MV/cm generated by optical rectification in LiNbO3 Appl. Phys. Lett. 98, 091106 (2011)

[11] **S. S. Dhilion, M.S. Vitiello, et al** The 2017 terahertz science and technology roadmap, J. Phys. D: Appl. Phys. 50, 043001 (2017)

[12] **T. Seifert, S. Jaiswal, et al** Ultrabroadband single-cycle terahertz pulses with peak fields of 300 kV cm^1 from a metallic spintronic emitter, Appl. Phys. Lett. 110, 252402(2017)

[13] **R. Rouzegar, A. Chekhov et al** Broadband Spintronic Terahertz Source with Peak Electric Fields Exceeding 1.5 MV/cm, PHYSICAL REVIEW APPLIED 19, 034018 (2023)

[14] **Q. Wu and X.-C. Zhang** Free-space electro-optic sampling of terahertz beams. Appl. Phys. Lett. 67, 3523 (1995)

[15] **D. M. Mittleman, R. H. Jacobsen, et al** Terahertz time-domain spectroscopy of water vapor, Appl. Phys. Lett. 64, 186-188 (1994)

[16] **S. M. Teo, B.K. Ofori, Okai, et al.** Invited Article: Single-shot THz detection techniques optimized for multidimensional THz spectroscopy, Review of Scientific Instruments 86, 051301 (2015)

[17] **Z. Jiang, X.C. Zhang** Electro-optic measurement of THz field pulses with a chirped optical beam, Applied physics letter 72, 1945 (1998)

[18] **Ashcroft, Neil W** Mermin, N. David, Solid State Physics (1976)

[19] **T.Seifert, S.Jaiswal, U.Martens, et al.** Efficient metallic spintronic emitters of ultrabroadband terahertz radiation, Nature Photon 10, 483–488 (2016)

[20] **S.M. Rouzegar et al** Laser-induced terahertz spin transport in magnetic nanostructures arises from the same force as ultrafast demagnetization, Phys. Rev. B 106, 144427 (2022)

[21] **E.Saitoh, M.Ueda et al.** Conversion of spin current into charge current at room temperature: Inverse spin-Hall effect, Appl. Phys. Lett. 88, 182509 (2006)

[22] **J. D. McMullen** Analysis of compression of frequency chirped optical pulses by a strongly dispersive grating pair, Appl. Opt. 18, 737-741 (1979)

[23] **Novotny and Hecht** Principles of nano-optics. Cambridge University Press (2006)

[24] **W. Demtröder** Experimentalphysik 3, Springer (2005)

[25] **M. Born and E. Wolf** Principles of Optics. New York: Cambridge University Press, 7th edition (1999)

[26] **Ursula Keller** Ultrafast Lasers: A Comprehensive Introduction to Fundamental Principles with Practical Applications. Springer (2021)

[27] **Edmond B. Treacy** Optical Pulse Compression With Diffraction Gratings. IREE Journal of Quantum Electronics, Vol QE-5, No. 9 (1969)

[28] **E. Martinez, J. P. Gordon, R. L. Fork** Negative group-velocity dispersion using refraction, J. Opt. Soc. Am. A 1 (10), 1003–1006 (1984)

[29] **E. Hecht** Optics, Fourth Edit, Pearson Higher Education (2003)

[30] **J. Nötzhold** Dissertation: Ultraschnelle Entmagnetisierung Laserangeregter Ferromagneten untersucht mit zeitaufgelöster Terahertz-Emissions-Spektroskopie, Uni Konstanz (2007)

[31] **P. Planken, H. Nienhuys et al** Measurement and calculation of the orientation dependence of terahertz pulse detection in ZnTe. J. Opt. Soc. Am. B 18, 313 (2001)

[32] **R. W. Boyd** Nonlinear Optics. Academic Press (1992)

[33] **T. Kampfrath** Dissertation: Charge-Carrier Dynamics in Solids and Gases Observed by Time-Resolved Terahertz Spectroscopy. FU Berlin (2005)

[34] **T. Kampfrath, J. Nötzold et al** Sampling of broadband terahertz pulses with thick electro-optic crystals, Appl. Phys. Lett. 90, 231113 (2007)

[35] **T. Kampfrath, D. Beggs et al** Complete response characterization of ultrafast linear photonic devices, Optics Letters, Vol. 34, No. 21 (2009)

[36] **J. Proakis, D. Manolakis**, Digital Signal Processing, 4th ed., Prentice Hall (2006)

[37] **Planken, Paul CM, et al.** Measurement and calculation of the orientation dependence of terahertz pulse detection in ZnTe, JOSA B 18.3, 313-317 (2001)

[38] **Leitenstorfer et al.** Detectors and sources for ultrabroadband electro-optic sampling: Experiment and theory. Appl. Phys. Lett. 74, 1516 (1999)

[39] **Eléonore Roussel, Christophe Szwaj, et al** Phase Diversity Electro-optic Sampling: A new approach to single-shot terahertz waveform recording, Light Sci Appl 11, 14 (2022)

[40] **F.G. Sun, et al.** Analysis of terahertz pulse measurement with a chirped probe beam, Appl. Phys. Lett. 73, 2233 (1998)

[41] **X.Y. Peng, et al.** To realize the optimal probe pulse length for detection of pulsed terahertz signal with spectral-encoding technique, Appl. Phys. Lett. 98, 231111 (2011)